remote sensing

MDPI

Article

An Empirical Radiometric Intercomparison Methodology Based on Global Simultaneous Nadir Overpasses Applied to Landsat 8 and Sentinel-2

Jorge Gil [1,*], Juan Fernando Rodrigo [2], Pablo Salvador [2], Diego Gómez [2], Julia Sanz [2] and Jose Luis Casanova [2]

[1] Independent Researcher, 47011 Valladolid, Spain
[2] Remote Sensing Laboratory (LATUV), University of Valladolid, Paseo de Belen 11, 47011 Valladolid, Spain; juanfernando.rodrigo@alumnos.uva.es (J.F.R.); pablo@latuv.uva.es (P.S.); diego@latuv.uva.es (D.G.); julia@latuv.uva.es (J.S.); jois@latuv.uva.es (J.L.C.)
* Correspondence: jorge.gilg@deimos-space.com

Received: 11 June 2020; Accepted: 21 August 2020; Published: 24 August 2020

Abstract: The Simultaneous Nadir Overpass (SNO) method was developed by the NOAA/NESDIS to improve the consistency and quality of climate data acquired by different meteorological satellites. Taking advantage of the reduced impact induced by the Bidirectional Reflectance Distribution Function (BRDF), atmospheric effects, illumination and viewing geometries during an SNO, we created a sensor comparison methodology for all spectral targets. The method is illustrated by applying it to the assessment of data acquired by the Landsat 8 (L8), Sentinel-2A (S2A), and Sentinel-2B (S2B) optical sensors. Multiple SNOs were identified and selected without the need for orbit propagators. Then, by locating spatially homogeneous areas, it was possible to assess, for a wide range of Top-of-Atmosphere reflectance values, the relationship between the L8 bands and the corresponding ones of S2A and S2B. The results yield high coefficients of determination for S2 A/B with respect to L8. All are higher than 0.980 for S2A and 0.984 for S2B. If the S2 band 8 (wide near-infrared, NIR) is excluded then the lowest coefficients of determination become 0.997 and 0.999 from S2A and S2B, respectively. This methodology can be complementary to those based on Pseudo-Invariant Calibration Sites (PICS) due to its simplicity, highly correlated results and the wide range of compared reflectances and spectral targets.

Keywords: cross-calibration; interoperability; Landsat-8 OLI; radiometric calibration; Sentinel-2 MSI; Simultaneous Nadir Overpasses

1. Introduction

The growing number of Earth Observation (EO) satellites reflects the societal demand of products and services based on remote sensing data [1]. To address the questions of how and to what extent different data sources can be used for a given product or service, and how to perform its harmonization, it is necessary to execute an assessment of data interoperability [2]. Calibration and cross-calibration processes are essential to ensure data quality, functionality and interoperability [3,4]. Post-launch calibration and validation activities are important for all optical sensors and essential for those which lack on-board calibration systems [5].

Pseudo-Invariant Calibration Sites (PICS) based methodologies have been widely used for cross-calibration [6]. These methodologies require Bidirectional Reflectance Distribution Function (BRDF) modelization [7,8] and are influenced by the atmosphere [9,10], while their results are restricted to a limited range of reflectances [11,12].

One of the most used techniques for cross-calibration and inter-calibration is the Simultaneous Nadir Overpass (SNO) methodology [13–18] developed by the National Environmental Satellite, Data, and Information Service (NESDIS) of the National Oceanic and Atmospheric Administration (NOAA) more than a decade ago [19].

SNO-based methodologies consist on the direct inter-comparison and subsequent adjustment of measurements obtained by sensors that fly on-board satellites when these sensors observe the same area of the Earth's surface in a very short time interval between acquisitions (Inter-Acquisition Time Gap, IATG) [3,14,20]. The key assumption behind the SNO is that when two different optical sensors acquire the same area nadir pointing and simultaneously, the BRDF, illumination geometry, viewing geometry and atmospheric influence on the measurements are equal for both observations [3,14,20], allowing the direct study of the compared radiometric performance of both sensors [3,20].

With the purpose of minimizing the aforementioned drawbacks in the PICS methodology and to simplify the process, we introduce a methodology based on multiple Simultaneous Nadir Overpasses (SNOs). In the frame of this work, we created a sensor comparison methodology for all spectral targets. We then used it to analyze the radiometric interoperability of data provided by the optical sensors on board the Sentinel-2A (S2A), Sentinel-2B (S2B) and Landsat 8 (L8) satellites. These sensors were chosen, due to their similarity in terms of spectral bands, spatial resolutions, and the interest of the earth-observation community in making them interoperable [4,21,22]. Firstly, this article presents a method to identify SNOs without using orbit propagators. Secondly, a technique is proposed to find spatially homogeneous areas to extract radiometric statistics. These data are analyzed and refined to discuss sensor interoperability and harmonization based on the compared Top-Of-Atmosphere (TOA) reflectances. The conclusions highlight the good radiometric correlation between L8 and S2 and the methodology consistency when compared with a PICS-based one.

2. Materials and Methods

The study time frame ranged from 2015-07-04 to 2019-11-05 with a worldwide scope. Most of the metadata needed, like image geometries, acquisition times and ground tracks, were available on the United States Geological Survey (USGS) (https://earthexplorer.usgs.gov/) and Copernicus Open Access Hub (http://scihub.copernicus.eu). S2 A/B data were L1C TOA reflectance products, and for L8, the Collection 1, Tier 1, of calibrated TOA reflectance products (L1TP). Both product sets are found ortho-rectified to the Universal Transverse Mercator projection (UTM/WGS84) and available on the same websites mentioned above [23,24].

2.1. Satellite Sensors

L8 was launched on 11 February 2013, from the Vandenberg Air Force Base in a circular sun-synchronous orbit with 16 days of repeat cycle, an altitude of ~705 km and an orbit plane inclination of 98.2°. It carries the Operational Land Imager (OLI) and the Thermal Infrared Sensor (TIRS) scientific instruments which have both a 15° field of view (FOV), providing a ~185 km swath. The OLI payload has nine spectral bands in the visible to near-infrared (VNIR) and short-wave infrared (SWIR) range with a spatial resolution of 30 m for bands 1 to 7 and 9, while the resolution of the panchromatic band (band 8) is 15 m [25].

The S2 mission is part of the Copernicus Program of the European Commission for global land surface monitoring and coastal waters. Currently, the S2 program consists on a constellation of two satellites, S2A and S2B, which were launched on 23 June 2015 and 7 March 2017, respectively, from the Europe's spaceport near Kourou in French Guiana. They are located in a sun-synchronous orbit, sharing the same orbit plane of 98.6° inclination and with a 180° orbital phasing difference at ~786 km height [26]. Both satellites are equipped with the MultiSpectral Instrument (MSI) payload which, with a 20.6° FOV provides a swath of ~290 km. The repeat cycle is 10 days for each satellite or 5 days for combined use [26]. The MSI has 13 spectral bands in the VNIR and SWIR spectral domains with spatial resolutions of 10 m for bands 2 to 4 and 8, 20 m for the bands 5, 6, 7, 8A, 11, 12, and 60 m for the bands 1, 9 and 10 [23,26].

2.2. Ground Trajectory Determination and SNOs Finding

Finding SNOs required the ground track determination of each satellite and the associated time for each point on the track to define the *ground trajectories*. A method was developed to estimate ground trajectories without using orbit propagators. For L8, only OLI C1 L1TP product metadata data [27] was needed, while S2A and S2B required the full-cycle 143-orbit tracks published by the ESA in addition to the L1C product metadata [28]. In order to avoid errors induced by the usage of projections, we performed the calculations on the three-dimensional WGS84 Earth model.

2.2.1. Landsat 8 Ground Trajectories

According to the L8 product metadata, more than 99.8% of the samples have a roll angle value lower than 2×10^{-30}, the rest have a maximum value of 4×10^{-30} representing ~1.4 km and ~2.8 km of off-nadir distance on the ground, respectively [29]. We considered these distances negligible. Each scene center was, hence, deemed a point belonging to the ground track, which we built using geodesics. The scene center time was calculated as the middle time between the scene start and stop times. It was then interpolated along the geodesic to build the ground trajectory. An example is shown in Figure 1.

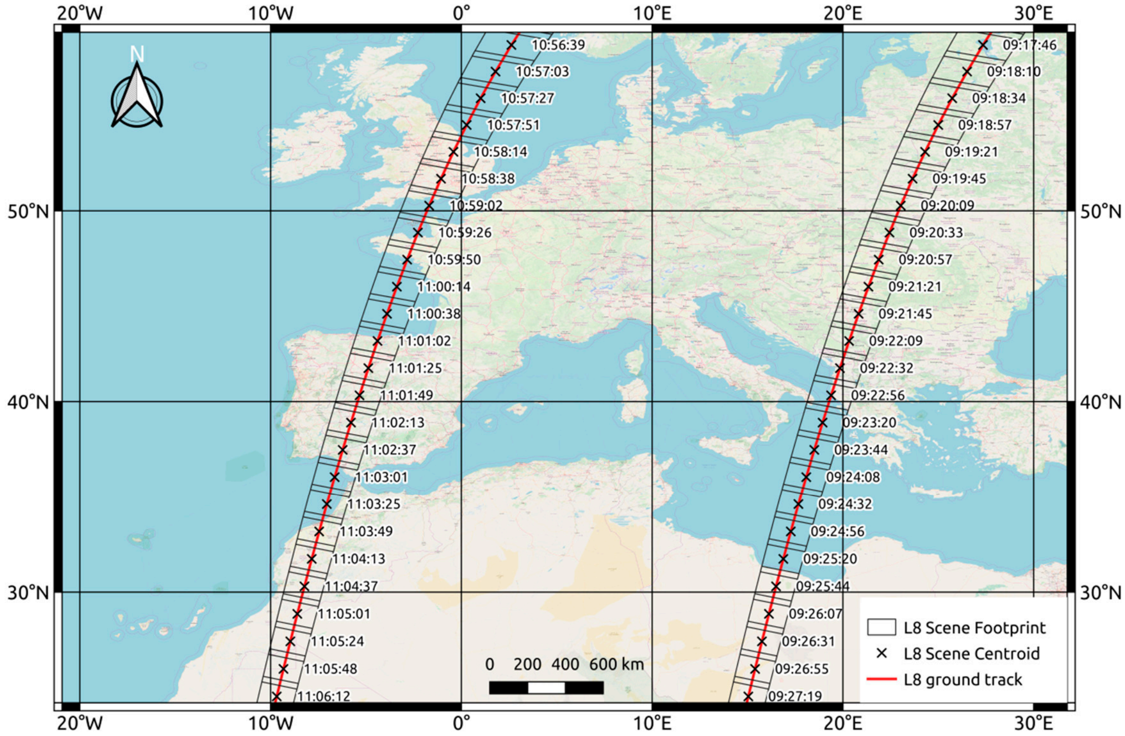

Figure 1. L8 ground tracks, scene footprints, centroids and center times over north Africa and Europe on 2017-08-20.

2.2.2. Sentinel-2 Ground Trajectories

S2A, S2B and L8 perform track maintenance [26,29–31], however, S2 products differed from L8 because they are tiled using the Military Grid Reference System (MGRS) [23,26]. This system has no relation to the orbits, therefore, we used the 143-orbit cycle ground tracks provided by ESA [28] for the calculation of the S2A and S2B ground trajectories. All S2 L1C products whose footprint intersected with the track of their corresponding cycle were then linked to their associated track segment. The granule sensing time metadata value of the product provided the time for the track segment. We obtained the ground trajectories for S2A and S2B by concatenating these time-labeled track segments and interpolating the time for each point on the track assuming that the granule sensing time corresponds to the first line of the granule. An S2A and S2B ground tracks example is shown in Figure 2.

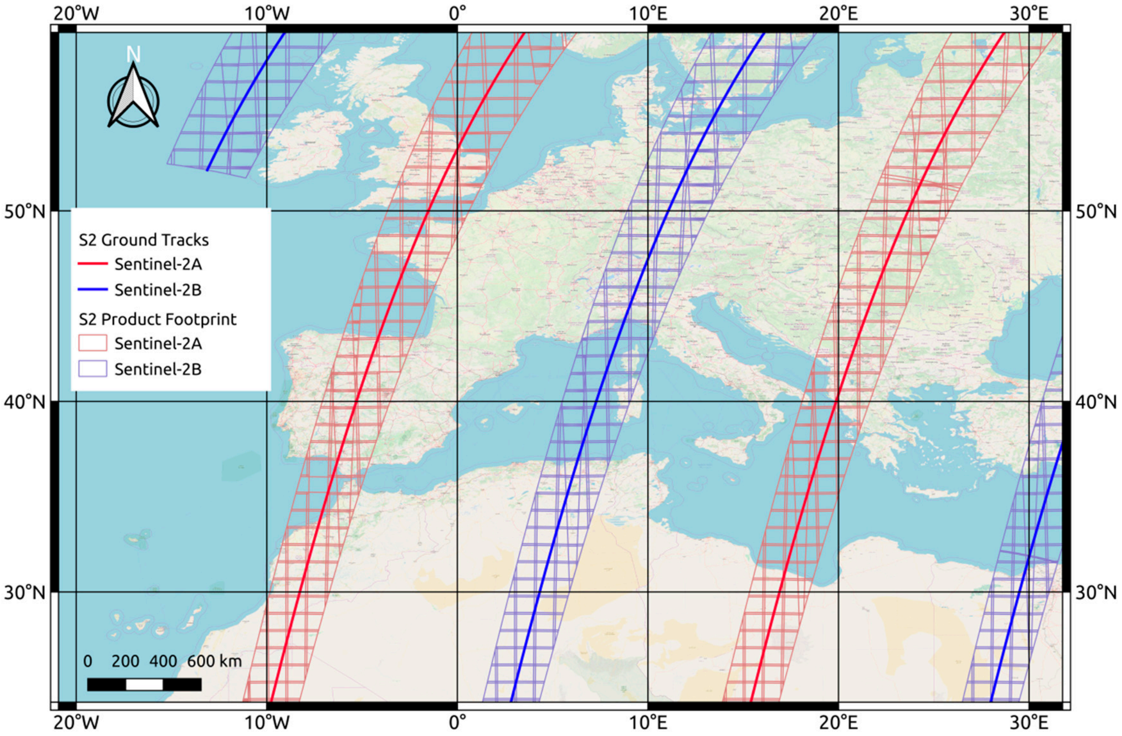

Figure 2. S2A and S2B ground tracks and L1C product footprints in the Military Grid Reference System (MGRS). Day 2017-08-20.

2.2.3. SNOs Determination

We define the perfect SNO as the event in which one sensor is orbiting exactly over the other at the same time. Under these conditions, both sensors virtually see the same nadir point with the same viewing and illumination angles. There are, then, two requirements, one spatial (orbit intersection) and the other temporal (simultaneity).

In practice, it is necessary to add tolerance to these requirements. In this work, we began by being strict in the geometric one. The orbit intersections are our starting points, while the tolerance is provided by the IATG. Once both have been established, an additional spatial tolerance is added as a radius, creating a circular area of study centered in the orbit intersection. It is worth noting that the spatial tolerance has a stronger influence on the viewing angles, while the temporal tolerance has a more significant impact on the solar angles.

The established ground trajectories were used to determine intersection points and IATGs of L8 and S2. We initially constrained the IATG to 24 h, obtaining 1397 S2A and 953 S2B overpasses with L8. Since the data extraction of each overpass required a significant amount of computing resources, we filtered out overpasses with an IATG longer than 30 min or whose S2 sample had more than 5% cloudiness value in the metadata. In this way, we reduced the number of overpasses to 96 S2A and 60 S2B (Appendix B).

This methodology required cloud-free areas. We set the cloudiness threshold in the S2 scene because it is smaller than the L8 one, and therefore, more restrictive. The cloudiness threshold value is the result of a trade-off between the chances of having clouds in the study area and the number of

SNOs. A cut-off value of 5% allows, approximately, three times more SNOs than the corresponding to 0%.

Once the intersection point and IATG were determined, the remaining element to complete our SNO identification was the radius. We used the radiometric data as they were obtained from the official providers without any kind of manipulation (e.g., resampling). For this reason, an SNO comprised a single L8 tile and a single S2 tile, therefore, the radius was calculated as the minimum distance from the intersection point to the polygon resulting from the intersection of both tiles. This radius was further reduced when necessary to avoid large water bodies, as shown in Figure 3. The study area is a circle centered in the ground track intersection point. This keeps the methodology compatible with satellites with opposed orbit directions.

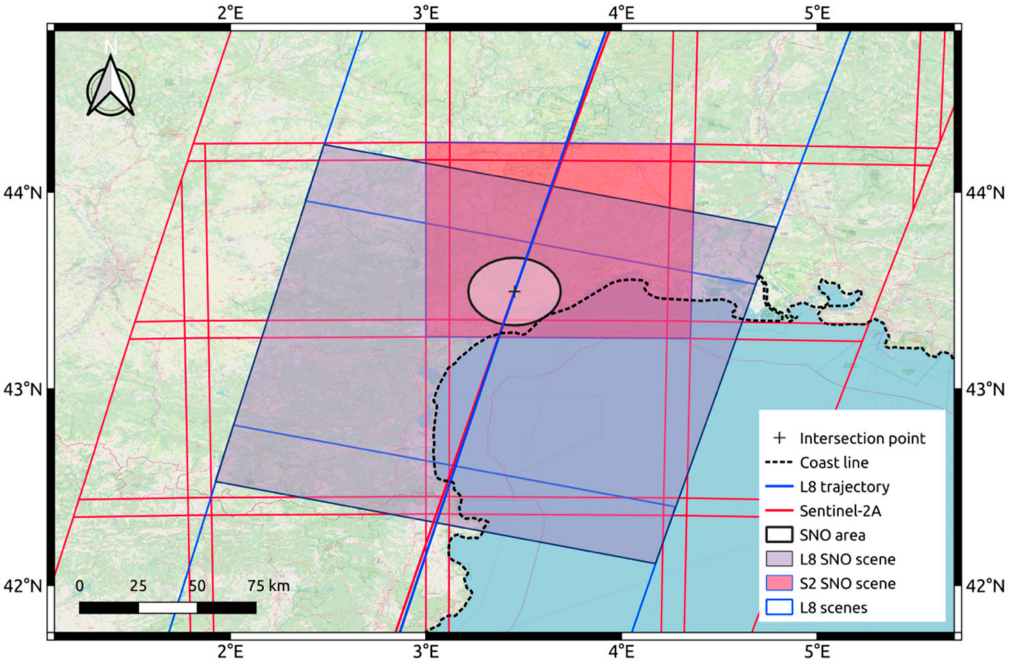

Figure 3. A Simultaneous Nadir Overpasse (SNO) near the Gulf of Lion (France) with its radius limited by the coastline. L8 scene LC08_L1TP_197030_20190722_20190801_01_T1, S2 scene S2A_MSIL1C_20190722T104031_N0208_R008_T31TEJ_20190722T110458.

Figures 4 and 5 show the world distribution of the SNOs areas used in our study. The circle size has been overscaled to ease the visualization.

2.3. Statistics Extraction

The coefficient of variation (CV) is an operator used as an indicator of the radiometric spatial uniformity [32]. The CV is defined as the ratio between the standard deviation and the average of values (Equation (1)).

$$CV = \frac{\sigma}{|\overline{x}|} \tag{1}$$

where $|\overline{x}|$ is the average value and σ its standard deviation.

Using the CV, an algorithm searched for spatially homogeneous areas [32,33] on each S2 band, and extracted TOA reflectance statistics for each individual area. The same areas were used to extract statistics on the corresponding bands of the L8 dataset. The distance to nadir, distance to the intersection of the ground trajectories, area, sun elevation and sun azimuth on the area centroid were also noted.

The bands used were all S2 VNIR and SWIR provided by the MSI with the exception of the water vapor (band 9), which was excluded due to the lack of a corresponding L8 OLI band [34]. The S2 cirrus band (band 10) was also excluded because the band does not provide useful ground data [35].

Although it could have been possible to several mosaic datasets to obtain larger SNO areas, it would have required merging, and in some cases, resampling. Our approach was strict into avoiding raster data manipulation; therefore, each SNO comprises only a pair of datasets: One L8 L1TP and one S2A or S2B L1C.

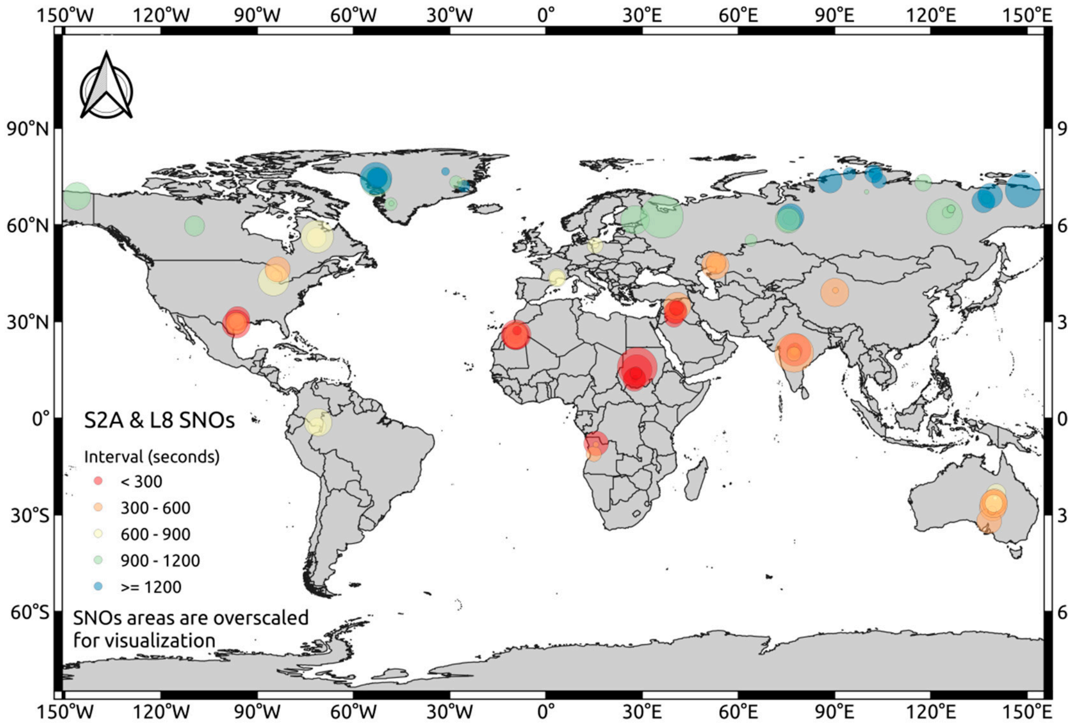

Figure 4. S2A and L8 SNOs distribution. Each point is a different SNO. The point size is related to the SNO size and the color represents the time gap between acquisitions. Areas overscaled for visualization.

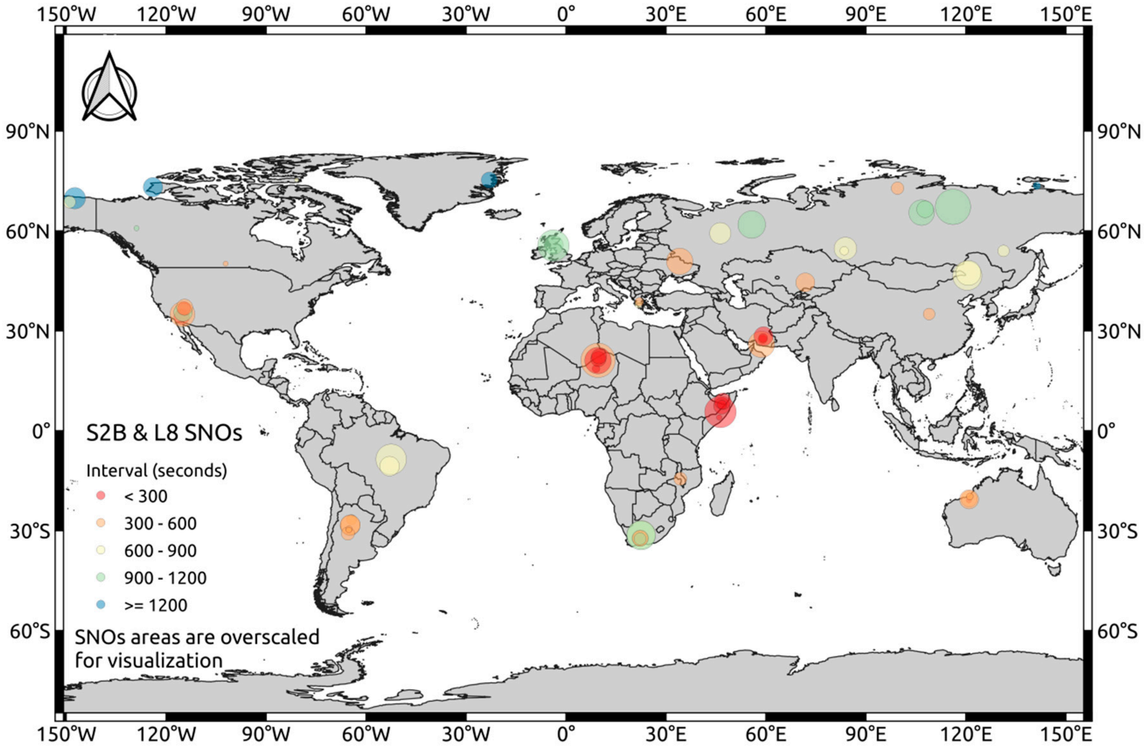

Figure 5. S2B and L8 SNOs distribution. Each point is a different SNO. The point size is related to the SNO size and the color represents the time gap between acquisitions. Areas overscaled for visualization.

For a given SNO, each pair of the selected bands was processed individually (Figure 6).

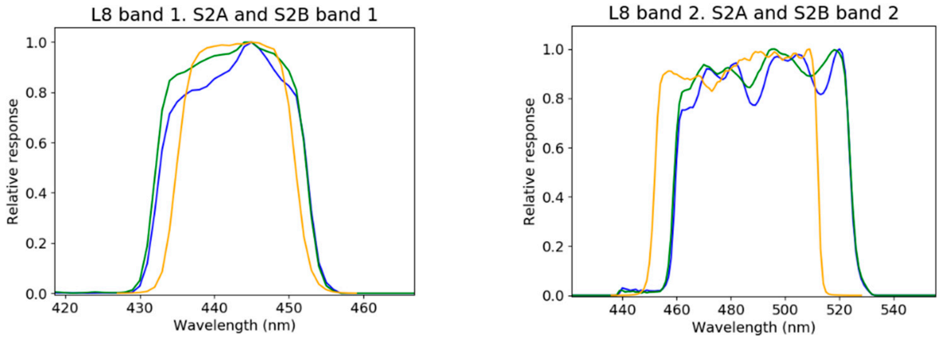

Coastal Aerosol Blue

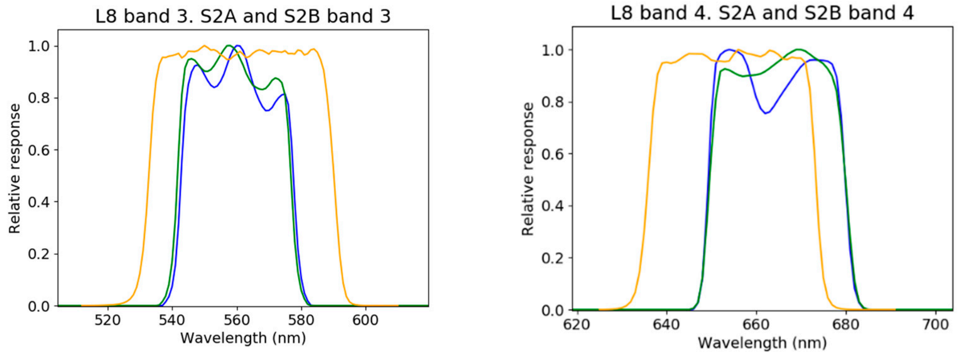

Green Red

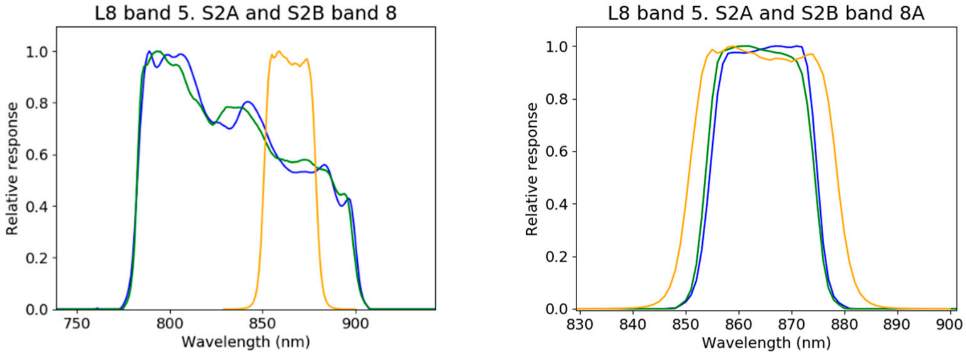

S2 Wide NIR and L8 Narrow NIR Narrow NIR

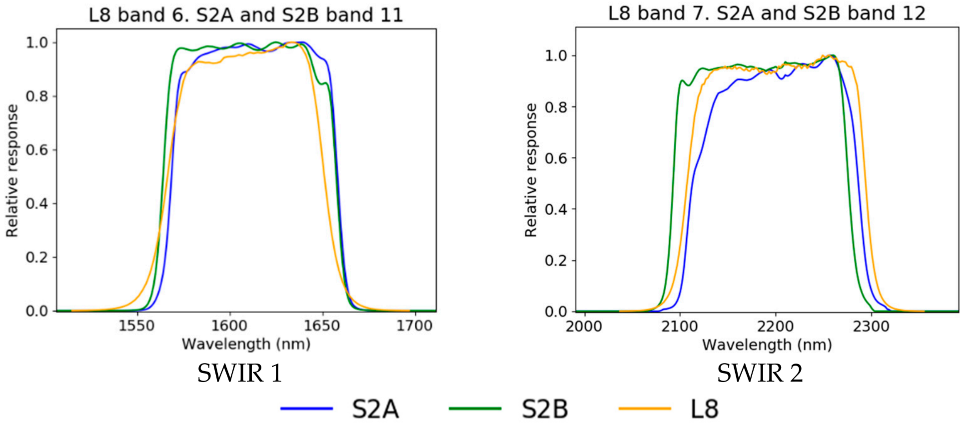

SWIR 1 SWIR 2

Figure 6. Comparison of relative spectral response (RSR) of S2A/B and L8 pair of bands selected for this study. NIR, near-infrared; SWIR, short-wave infrared.

2.3.1. Homogeneous Areas Creation

The S2 band was first convolved using the CV operator to obtain an image representing its spatial variability. The CV value corresponding to the percentile 1 of the sample was set as a threshold to binarize the CV image previously calculated. The pixels with values lower than the threshold were set to 1, and the remaining were set to 0. The erode operator [36,37] was then applied to reduce the size of the pixel clusters and to remove the smallest. The remaining clusters partially recovered their surface after applying a dilate operator [36,37] with a smaller kernel. Finally, the clusters were vectorized creating what we defined as Homogeneous Areas (HAs). For each SNO and S2 band, a set of Has was created.

We assumed that a HA in a higher resolution image is also homogeneous in a lower resolution one. For this reason, we choose the S2 bands for the Has creation since, with the exception of the coastal aerosol, the S2 bands have higher resolution than the L8. The use of a threshold from a percentile grants data from all samples. We reached the percentile value by trial and error, probing between 0.1 and 5.0. It was observed that the results had low sensitivity to this parameter. We expected the Has to minimize the possible effects of the resolution differences between the S2 and L8 bands, as well as small geometric errors. For the latter reason, the erode is stronger than the dilate; it creates a geometric margin-of-error distance for the HA. An example of the generation of homogeneous zones is shown in Figures 7 and 8.

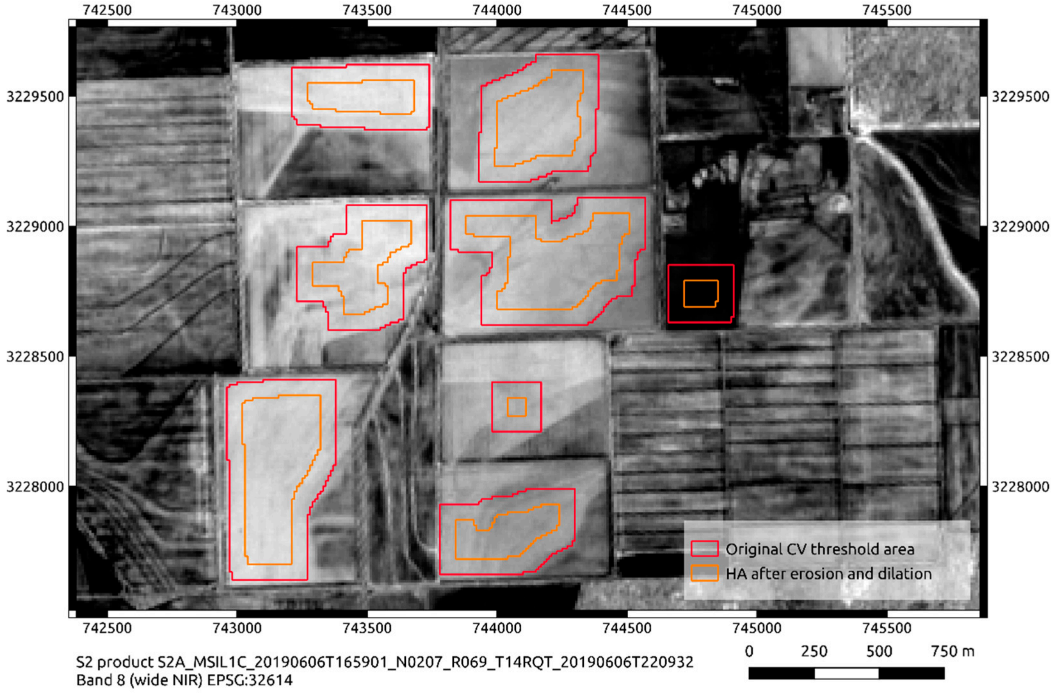

S2 product S2A_MSIL1C_20190606T165901_N0207_R069_T14RQT_20190606T220932
Band 8 (wide NIR) EPSG:32614

Figure 7. Original areas calculated using a coefficient of variation (CV) threshold value for the S2 wide NIR band in the scene S2A_MSIL1C_20190606T165901_N0207_R069_T14RQT_20190606T220932 and their corresponding Homogeneous Areas (Has), leaving a margin for small geometric differences between S2 and L8.

2.3.2. Statistics Retrieval

We noted the maximum, minimum, average and standard deviation of each pixel Digital Number (DN) and HA of the corresponding S2 and L8 bands. Following the restriction of maintaining the original raster values, the HA polygons, and not the images, were reprojected when the pair of SNO images were found in different projections. HAs smaller than nine OLI MS pixels (900 m^2) were removed from the study. Additionally, sun angles, pass-time, locations, centroid distance to nadir and intersection point were recorded. Each HA was an independent data point regardless of the SNO to which it belonged. They were kept separately, so the spectral differences stayed separate.

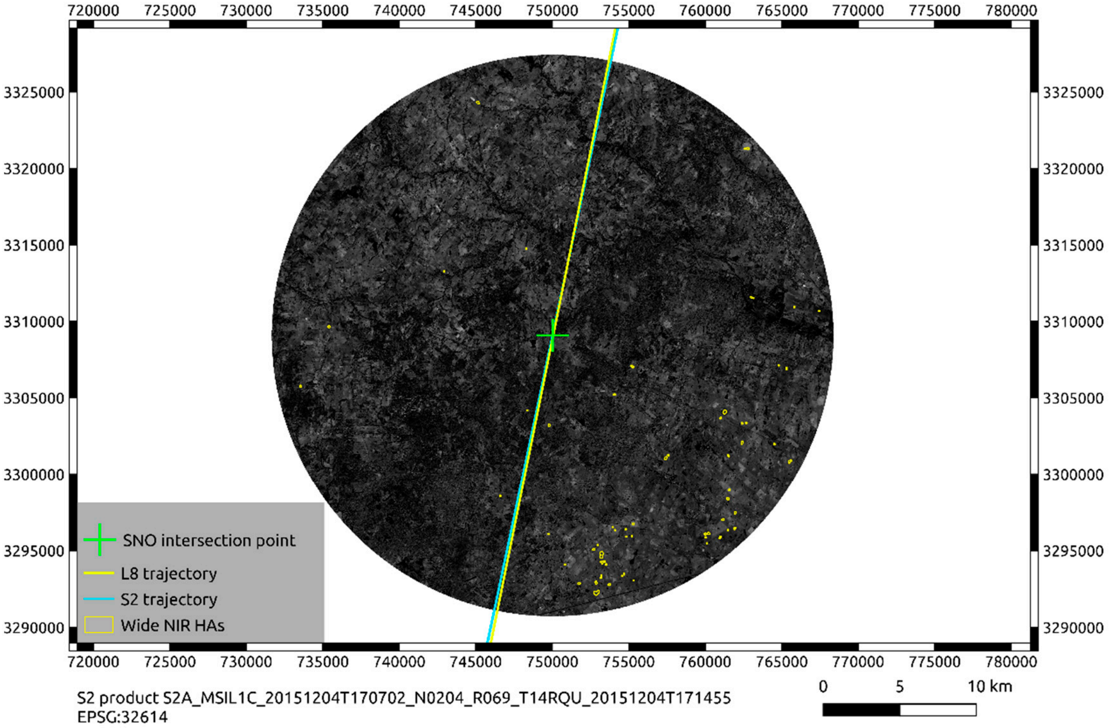

Figure 8. HAs obtained for the wide NIR band of the S2A_MSIL1C_20151204T170702_N0204_R069_T14RQU_20151204T171455 product.

2.4. Data Analysis

The S2 TOA reflectance was calculated applying the rescaling factor provided in the metadata to the S2 DNs, since the solar elevation across the scene has been already taken into account [38]. Following the product guide, we obtained the L8 TOA reflectance by applying the rescaling factors included in the metadata to the L8 DNs. Subsequently, these values were divided by the sine of the solar elevation at the HA centroid location at the L8 scene center time [39].

The L8 TOA reflectances were plotted versus the S2A and S2B TOA reflectances individually for each pair of corresponding bands, and a linear regression was calculated. Each SNO was represented with a different color, allowing the location of outliers and the identification of SNOs requiring visual inspection (Figure 9). The IATGs were, in general, too long to assume that cloudy areas were radiometrically stable. Shadow areas are solely illuminated by the atmosphere. For these reasons, cloudy and shadow areas were not used in this study (Figure 10). Scenes containing water flows and those containing perceptible atmospheric effects were also radiometrically dynamic (Figure 11), causing the presence of outliers. Only data points with justified anomalies were removed. The list of SNOs with valid HAs can be found in Appendix B.

The number of generated HAs largely differed depending on the SNO area texture. In order to balance their weight, we limited the number of HAs per SNO selecting the ones with the lowest standard deviation. No improvement was observed; therefore, the limitation was not used.

In the SNO used to illustrate B and C of Figure 11, L8 crossed over the intersection point 136 s after S2A. In cases like these, where anomalies are caused by the atmosphere, the entire SNO (all bands) is removed from the study.

A general schematic of the workflow followed for this study is shown in Figure 12.

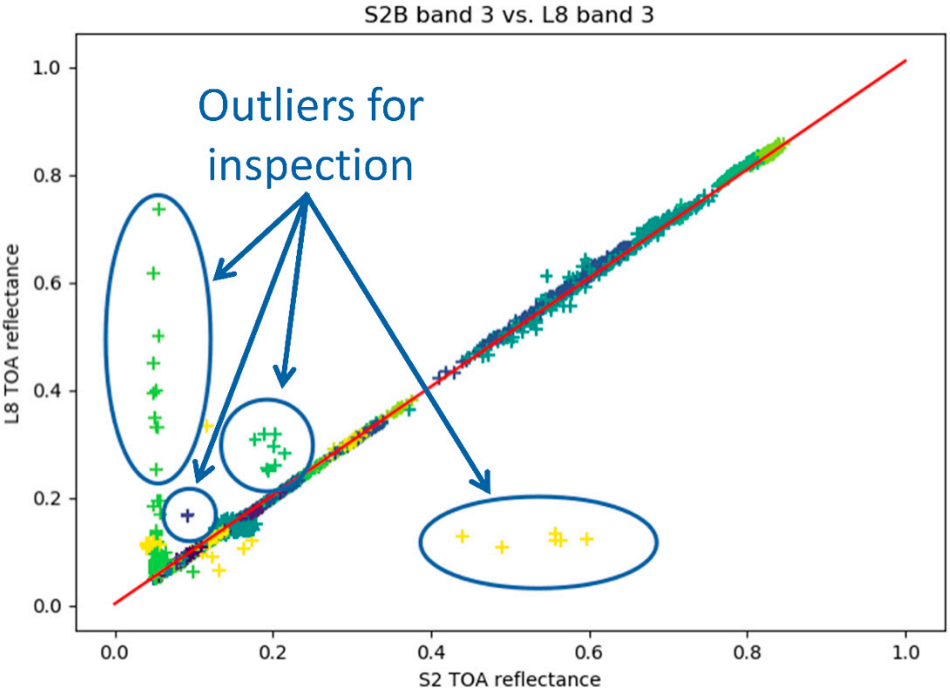

Figure 9. Outliers are identifying scene candidates for visual inspection. Each point is a different HA. Points with different colors belong to different SNOs. Red line is the linear regression.

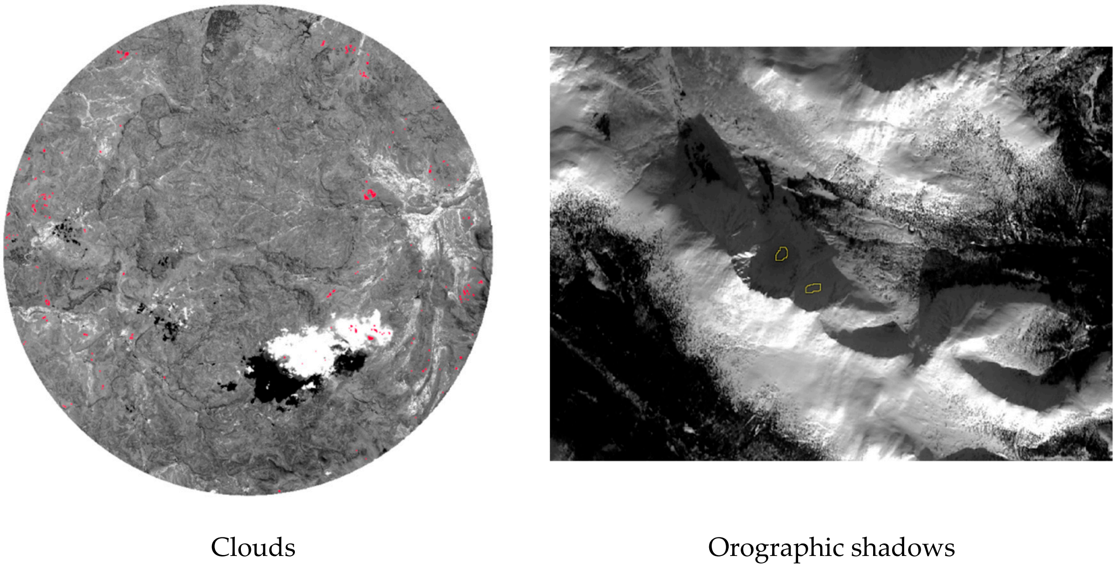

Figure 10. Cloudy and areas with orographic shadows discarded after inspection.

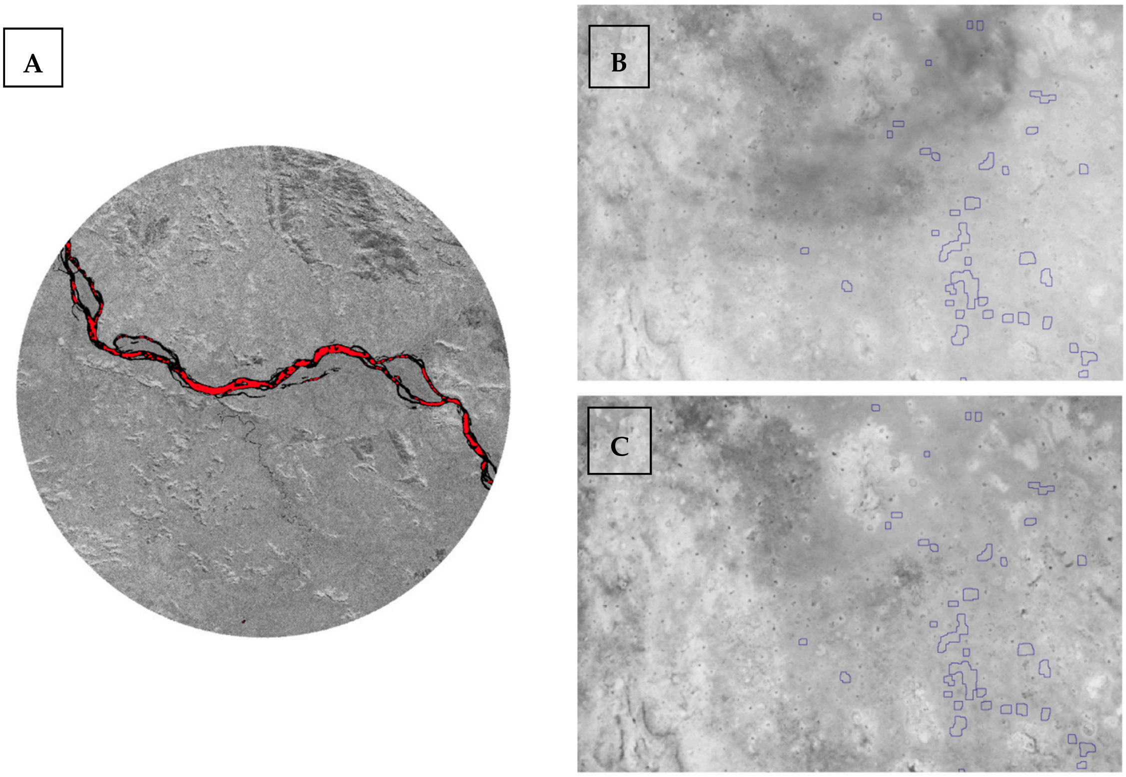

Water flows

Atmospheric effects

Figure 11. Examples of anomalies identified during the outlier inspection: HAs (red) over water flows in an S2B narrow NIR band (**A**) and visual differences in the SWIR2 band between an S2A (**B**) and an L8 (**C**) scenes caused by atmospheric effects, HAs in blue.

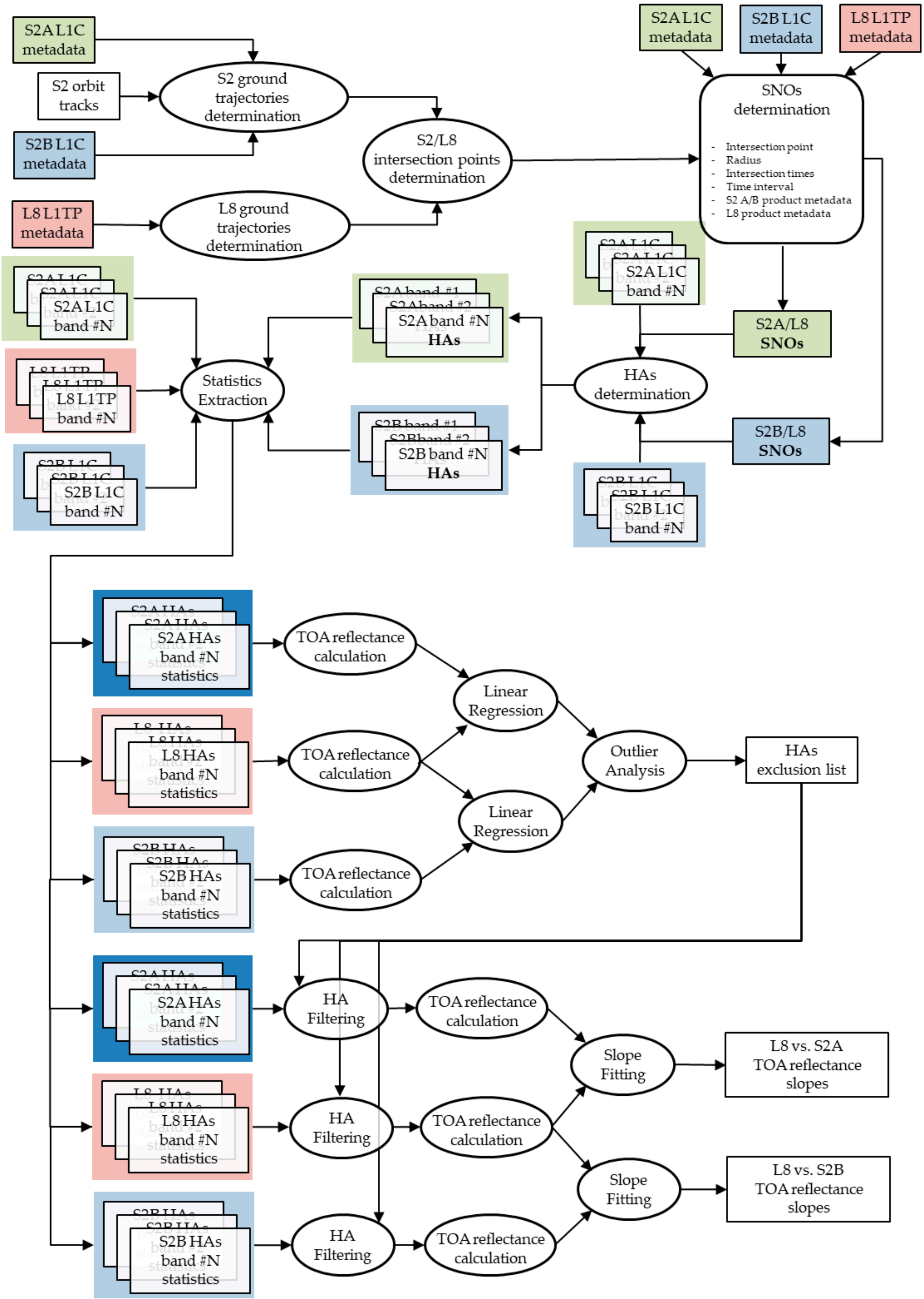

Figure 12. General workflow for SNOs methodology.

3. Results

3.1. Data Analysis Remarks

During the data analysis, we found that anomalies are very noticeable in the linear regression figures. As an example, Figure 13 shows how a smoke plume creates a salient outlier. Another interesting finding was the good behavior of the snow-covered slopes in different angles. Figure 14 shows HAs located on such surfaces whose reflectances stay aligned in the graph. It is worth noting that the reflectivity values are much higher than one, indicating the presence of the expected snow BRDF anisotropy.

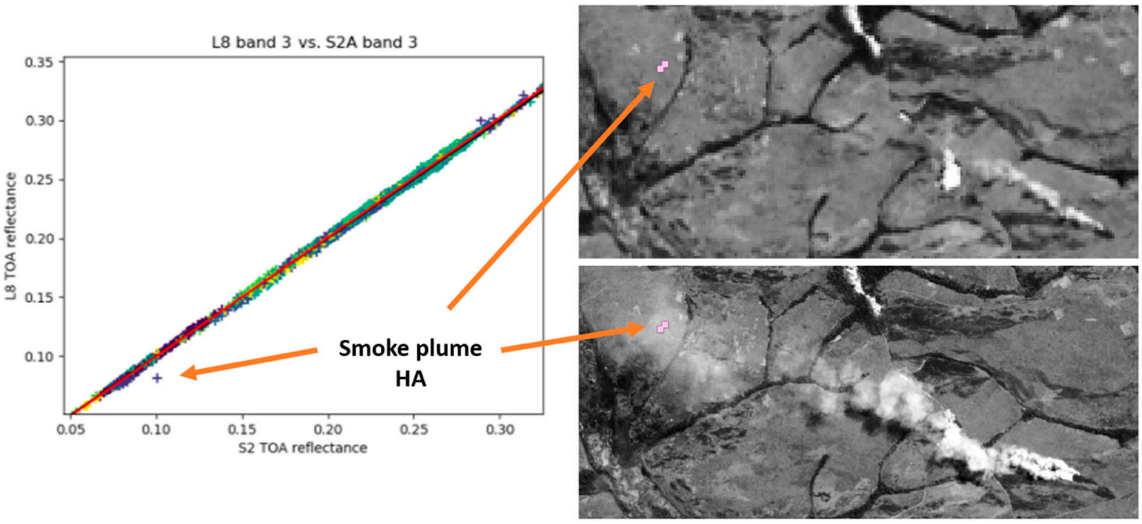

Figure 13. Outlier created by a smoke plume. Each point is a different HA. Points with different colors belong to different SNOs. Red line is the linear regression.

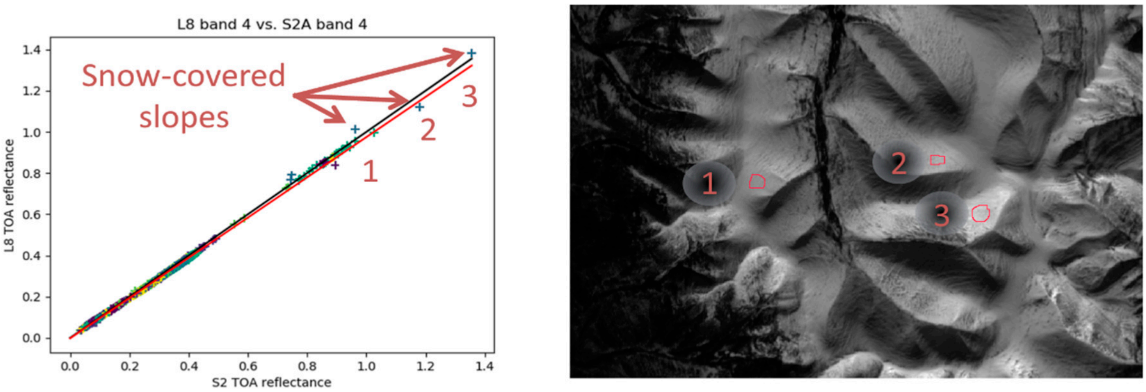

Figure 14. Response to highly anisotropic Bidirectional Reflectance Distribution Function (BRDF) where each point represents a different HA. Points with different colors belong to different SNOs. The red line indicates the linear regression and the black line is the slope 1.

3.2. Correlation with TOA Reflectances

A linear regression was applied to each band pair for S2 A/B and L8 TOA reflectance sets, obtaining the results presented in Tables 1 and 2. Appendix A shows the graphs of the linear regression for each band pair for S2 A/B and L8. The standard deviation of the residuals was the measure of the uncertainty used to create confidence intervals.

Table 1. Linear regression values for each band pair for L8 and S2A.

L8 vs. S2A					
S2 Band	**L8 Band**	**Band Name**	**Slope**	**Intercept**	**Coefficient of Determination**
1	1	Coastal Aerosol	0.99111	-9.307×10^{-4}	0.99993
2	2	Blue	0.99267	3.248×10^{-4}	0.99907
3	3	Green	1.01095	-1.441×10^{-3}	0.99969
4	4	Red	0.97671	-2.016×10^{-3}	0.99874
8A	5	Narrow NIR	0.99087	-3.732×10^{-4}	0.99953
8	5	Wide NIR	1.02380	1.470×10^{-2}	0.99115
11	6	SWIR 1	0.98953	-2.443×10^{-3}	0.99956
12	7	SWIR 2	1.00041	-3.116×10^{-3}	0.99964

Table 2. Linear regression values for each band pair for L8 and S2B.

L8 vs. S2B					
S2 Band	**L8 Band**	**Band Name**	**Slope**	**Intercept**	**Coefficient of Determination**
1	1	Coastal Aerosol	1.00396	-9.729×10^{-4}	0.99991
2	2	Blue	1.01424	-8.120×10^{-4}	0.99974
3	3	Green	1.02565	-3.433×10^{-3}	0.99973
4	4	Red	1.00034	-3.760×10^{-3}	0.99941
8A	5	Narrow NIR	1.00989	-2.867×10^{-3}	0.99942
8	5	Wide NIR	1.01025	1.909×10^{-2}	0.99381
11	6	SWIR 1	0.99641	-3.151×10^{-3}	0.99973
12	7	SWIR 2	0.98597	2.116×10^{-4}	0.99972

With the exception of the wide NIR band, all regressions produce offsets whose absolute values are lower than 0.38% with high coefficients of determination. We assumed then that all TOA reflectance products yield zero for zero signal, so we removed the degree of freedom corresponding to the intercept and repeated the process to obtain the final results presented in Tables 3 and 4. The corresponding graphs can be found in Appendix A.

Table 3. Linear regression values for each band pair (L8 and S2A) with zero intercept.

L8 vs. S2A				
S2 Band	**L8 Band**	**Band Name**	**Slope**	**Coefficient of Determination**
1	1	Coastal Aerosol	0.98911	0.99985
2	2	Blue	0.99402	0.99814
3	3	Green	1.00540	0.99931
4	4	Red	0.97124	0.99741
8A	5	Narrow NIR	0.98999	0.99907
8	5	Wide NIR	1.06036	0.97962
11	6	SWIR 1	0.98441	0.99906
12	7	SWIR 2	0.99299	0.99914

Excluding again the wide NIR band we found coefficients of determination higher than 0.997 and 0.999 for S2A and S2B, respectively.

3.3. Dependence from Other Variables

The linear fitting allowed us to analyze the correlation of the residual of each HA with the following variables:

- Average reflectance;
- Reflectance standard deviation;
- Solar elevation at the HA centroid;
- Solar azimuth at the HA centroid;
- HA centroid distance to nadir;
- HA latitude.

Table 4. Linear regression values for each band pair (L8 and S2B) with zero intercept.

L8 vs. S2B				
S2 Band	**L8 Band**	**Band Name**	**Slope**	**Coefficient of Determination**
1	1	Coastal Aerosol	1.00188	0.99980
2	2	Blue	1.01277	0.99948
3	3	Green	1.01872	0.99932
4	4	Red	0.99326	0.99867
8A	5	Narrow NIR	1.00428	0.99877
8	5	Wide NIR	1.04793	0.98434
11	6	SWIR 1	0.98985	0.99935
12	7	SWIR 2	0.98645	0.99943

The same analysis was performed using the aggregated residuals of complete SNOs with the acquisition date and IATGs. No correlation was found between the residuals and any of the listed variables. For this reason, no restriction was set on the radius or sun angles. The radius is solely limited by the restrictions imposed by the SNO definition itself (Section 2.2.3). Being OLI and MSI pushbroom, the HA to nadir distances account for the across-track viewing angle. The lack of correlation between residuals and distances is the reason why we left the distance (or across-track angle) unconstrained in our dataset. Four examples are shown in Figure 15.

Figure 16 shows the distribution of HA distance to nadir differences between L8 and S2 A/B for each HA. It is worth noting that it is centered, symmetric and bell-shaped. The average is ~2.1 m with a standard deviation of 199.2 m, approximately 4.5×10^{-20} of across-track viewing angle difference error ($\pm 3\sigma$), that we can consider negligible.

No HA was seen with an across-track angle larger than 3.9°. For the purpose of this work, the viewing zenith angles can be considered virtually the same as the across-track angles. Similarly, the viewing azimuth angle difference is virtually the difference between orbit plane inclinations, ~0.4° in this case, recalling that S2A and S2B share the same orbit plane. It is worth highlighting that the difference in viewing azimuth angles becomes irrelevant as the HA distance to nadir diminishes.

3.4. Ground Classes Distribution

Since SNOs can be located anywhere in the world and HAs are randomly distributed within them, it was considered appropriate to inspect the distribution of ground classes across HAs. The Copernicus Global Land Cover Layers collection 2 at 100 m resolution (CGLS-LC100) [40] was used for this purpose. The CGLS-LC100 has the following features [40]:

- Derived from PROBA-V satellite observations for the 2015 reference year;
- Discrete classification with 23 classes;
- 100 m spatial resolution;
- An overall 80% accuracy.

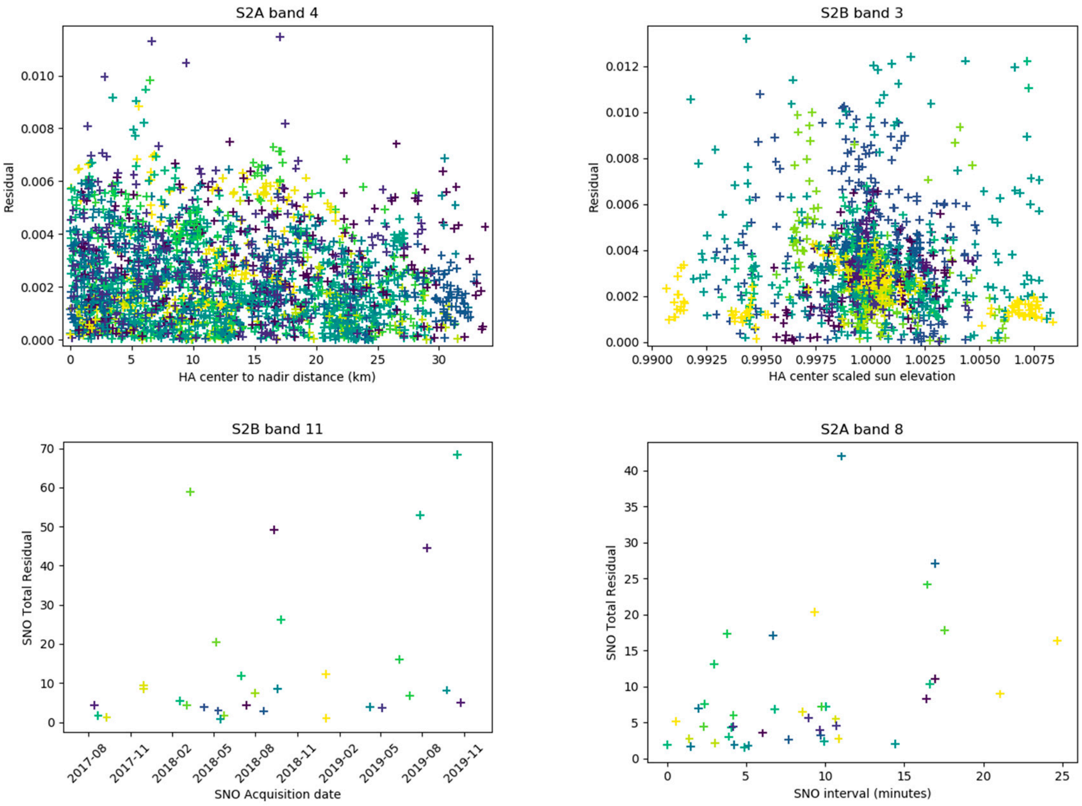

Figure 15. From left to right and top to bottom, the figures represent the residual values against the distance to nadir, sun elevation, acquisition date and Inter-Acquisition Time Gap (IATG). Each point is a different HA. Points with different colors belong to different SNOs.

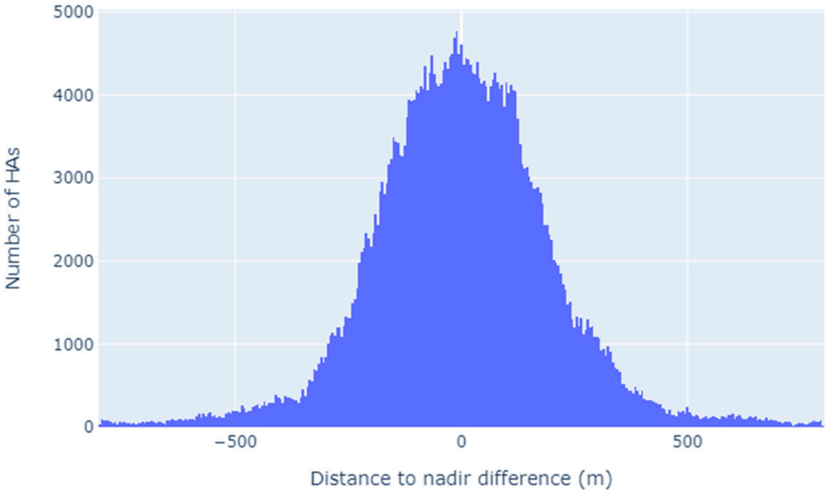

Figure 16. HA distance to nadir differences distribution (L8–S2).

Table 5 specifies each CGLS-LC100 class type used in this work, as well as its corresponding color and ID. Figure 17 shows the class distribution across HAs per S2 satellite and band. It is worth recalling that HAs were extracted from MSI data.

Table 6 and Figure 18 show, as an example, the regressions of the S2A/B band 4 when they are calculated using the most frequent classes separately. For convenience, the figure and data obtained with no class discrimination are also included.

Table 5. Legend for the 23 discrete classes of CGLS-LC100.

Color	Class ID	Class Name
🟫	22	Oceans, seas. Can be either fresh or salt-water bodies.
🟦	21	Open forest, not matching any of the other definitions.
🟦	20	Open forest, mixed.
🟨	19	Open forest, deciduous broadleaf. Top layer—trees 15–70% and second layer—mixed of shrubs and grassland, consists of seasonal broadleaf tree communities with an annual cycle of leaf-on and leaf-off periods.
🟨	18	Open forest, deciduous needle leaf. Top layer—trees 15–70% and second layer—mixed of shrubs and grassland, consists of seasonal needle leaf tree communities with an annual cycle of leaf-on and leaf-off periods.
⬜	17	Open forest, evergreen broadleaf. Top layer—trees 15–70% and second layer—mixed of shrubs and grassland, almost all broadleaf trees remain green year-round. Canopy is never without green foliage.
⬜	16	Open forest, evergreen needle leaf. Top layer—trees 15–70% and second layer—mixed of shrubs and grassland, almost all needle leaf trees remain green all year. Canopy is never without green foliage.
🟥	15	Closed forest, not matching any of the other definitions.
🟥	14	Closed forest, mixed.
🟥	13	Closed forest, deciduous broadleaf. Tree canopy > 70%, consists of seasonal broadleaf tree communities with an annual cycle of leaf-on and leaf-off periods.
🟫	12	Closed forest, deciduous needle leaf. Tree canopy > 70%, consists of seasonal needle leaf tree communities with an annual cycle of leaf-on and leaf-off periods.
🟫	11	Closed forest, evergreen broadleaf. Tree canopy > 70%, almost all broadleaf trees remain green year-round. Canopy is never without green foliage.
🟪	10	Closed forest, evergreen needle leaf. Tree canopy > 70%, almost all needle leaf trees remain green all year. Canopy is never without green foliage.
🟪	9	Moss and lichen.
🟥	8	Herbaceous wetland. Lands with a permanent mixture of water and herbaceous or woody vegetation. The vegetation can be present in either salt, brackish, or freshwater.
🟥	7	Permanent water bodies. Lakes, reservoirs, and rivers. Can be either fresh or salt-water bodies.
🟩	6	Snow and ice. Lands under snow or ice cover throughout the year.
🟩	5	Bare/sparse vegetation. Lands with exposed soil, sand, or rocks and never has more than 10% vegetated cover during any time of the year.
🟧	4	Urban/built up. Land covered by buildings and other manufactured structures.
🟧	3	Cultivated and managed vegetation/agriculture. Lands covered with temporary crops followed by harvest and a bare soil period (e.g., single and multiple cropping systems). Note that perennial woody crops will be classified as the appropriate forest or shrubland cover type.
🟦	2	Herbaceous vegetation. Plants without persistent stem or shoots above ground and lacking definite firm structure. Tree and shrub cover is less than 10%.
🟦	1	Shrubs. Woody perennial plants with persistent and woody stems and without any defined main stem being less than 5 m tall. The shrub foliage can be either evergreen or deciduous.
⬛	0	Unknown

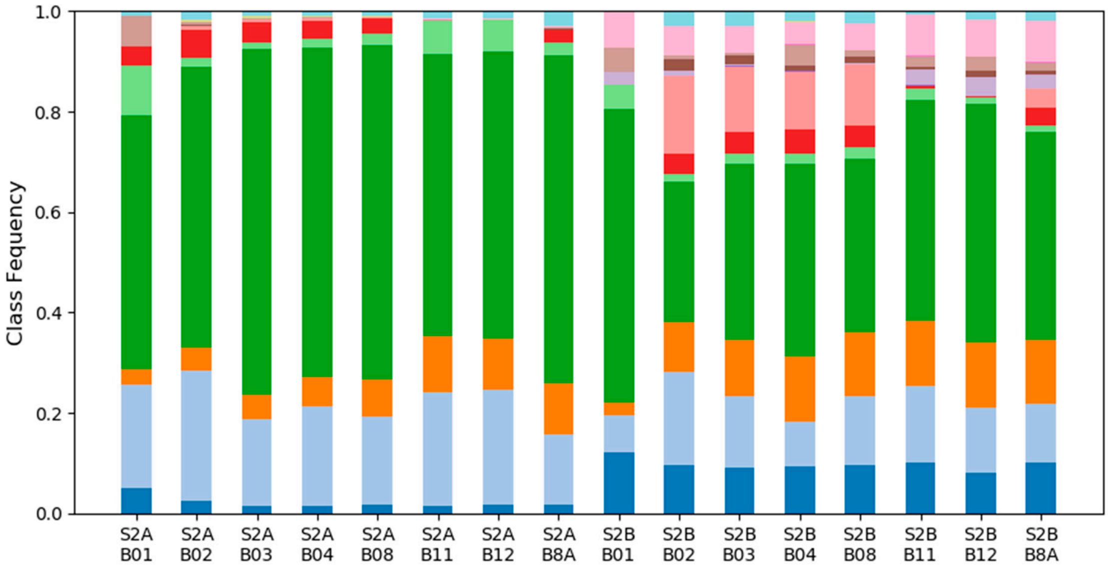

Figure 17. Class distribution of CGLS-LC100 across HAs per band of S2A and S2B satellites.

Table 6. Linear fitting slopes for S2 band 4 and L8 band 4 for the most frequent classes.

MSI Band 4, OLI Band 4 (Red). Most Frequent Classes					
Satellite	**Slope**	**Correlation Index**	**Number of HAs**	**Class**	**Class Description**
S2A **S2B**	0.97124 0.99444	0.99741 0.99873	2376 1702	all	All classes
S2A **S2B**	0.96765 0.97898	0.99310 0.99876	1558 655	5	Bare/sparse vegetation
S2A **S2B**	0.97106 0.98698	0.99599 0.99378	142 221	3	Cultivated and managed vegetation/agriculture
S2A **S2B**	0.97171 0.99318	0.99511 0.99932	471 152	2	Herbaceous vegetation
S2A **S2B**	0.97181 0.97378	0.99857 0.99667	33 158	1	Shrubs

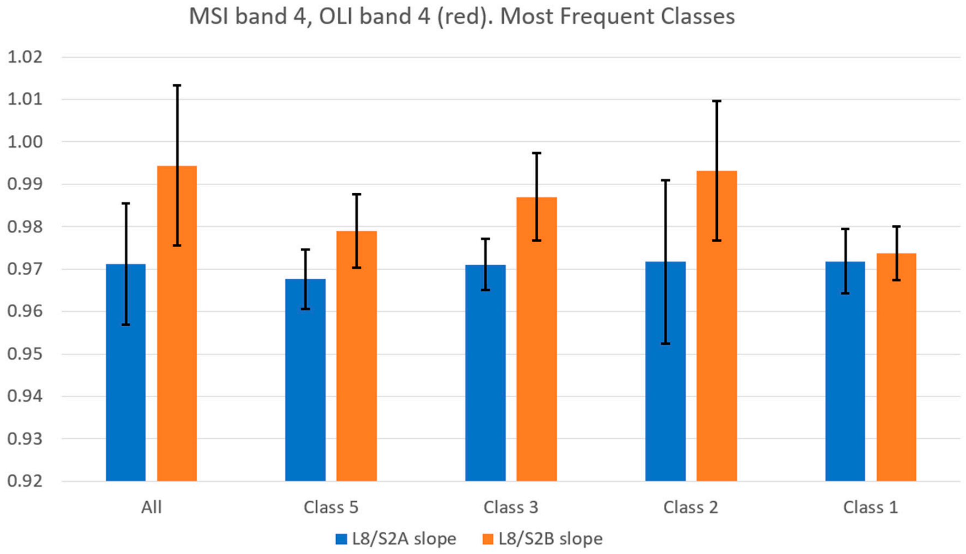

Figure 18. Linear fitting slopes for S2 band 4 and L8 band 4 for the most frequent classes (representation of Table 6). Confidence interval ±3σ.

Regression figures corresponding to Table 6 can be found in Appendix C.

4. Discussion

In this study, we identified SNOs across the globe using a ground-agnostic method. As a result, for each pair S2A/L8 and S2B/L8, diverse ground types were targeted (Figures 4 and 5). Unlike PICS-based methodologies where the targets are in well-defined, characterized and fixed locations [7,9,41], the proposed method prioritizes the intersection point regardless of its location on the Earth, with a limited IATG of 30 min. The method allows a strongly empirical approach, with no need for atmospheric or BRDF correction. Despite the spectral diversity of the study area, the coefficients of determination between L8 and S2 bands (wide NIR band excluded) were higher than 0.997 (S2A) and 0.999 (S2B). The SNO plus Has technique provides a wide range of reflectances for study, often from less than 0.1 to values close to 1 (Appendix A), while PICS-based methodologies are restricted to a reduced set [11,12].

The ground classes breakdown (Figure 17) shows the presence of both arid and vegetated classes in the samples. The class that includes deserts, defined as "bare/sparse vegetation", is the most frequent. It is followed by "herbaceous vegetation", "cultivated and managed vegetation/agriculture", "shrubs", and "herbaceous wetland". The frequency distribution of these vegetated classes differs for each satellite and band. "Herbaceous vegetation" is more strongly represented in S2A, while "herbaceous wetland" is its counterpart in S2B (Figure 17). These differences can be attributable to the world distribution of SNOs for each satellite. No significant statistic impact is expected to arise from this disparate distribution of similar vegetated classes using the SNO-HA method.

Helder et al. [4] collected the S2A/MSI and absolute calibration results obtained through different models and combined them in a metric that should serve to remove any systematic errors within the models and provide for a per-model comparison [4]. We added the results provided by our method to the figure published in the aforementioned work (Figure 19).

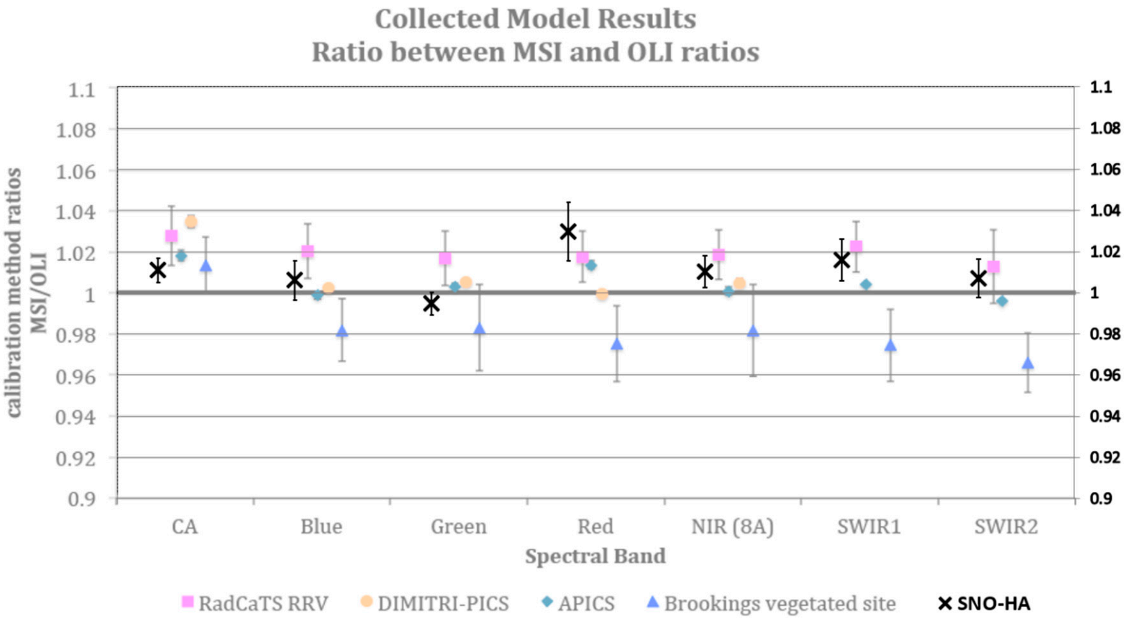

Figure 19. Comparison between S2A and L8 slopes from Table 3 (SNO-HA method) represented by solid black crosses and Helder et al. [4] results (represented by faded colors). SNO-HA confidence interval ±3σ.

The Copernicus Sentinel-2 Mission Performance Centre (MPC) also published ratios as radiometric validation indicators using Rayleigh atmospheric backscattering over deep ocean sites, in-situ data, spectrally characterized PICS and comparison with other sensors (S2A/MSI vs. OLI, S2B/MSI vs. OLI and S2B/MSI vs. S2A MSI) over Libya-4 [42]. Thus, Figures 20 and 21 show our results compared to the ones obtained in the latter study.

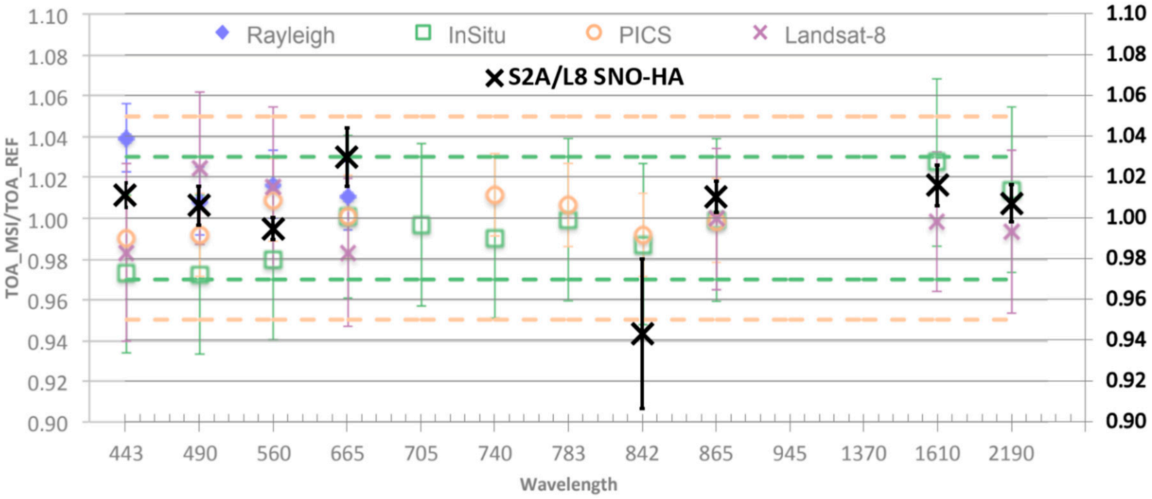

Figure 20. S2A vs. L8 slopes from Table 3 (SNO-HA method) solid black crosses over the results obtained through different models by MPC with S2A/MSI which are shown faded. SNO-HA confidence interval ±3σ.

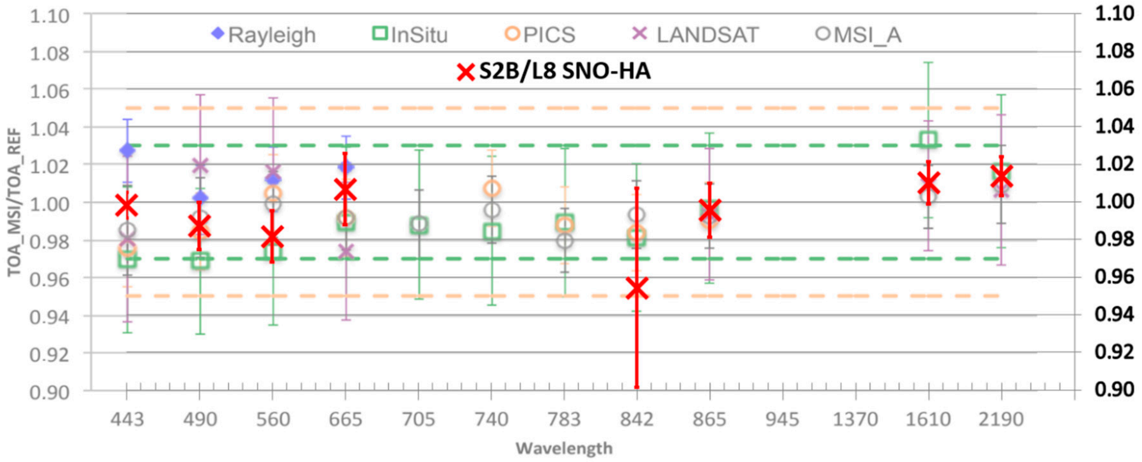

Figure 21. S2B vs. L8 slopes from Table 4 (SNO-HA method) solid red crosses over the results obtained through different models by MPC for S2B/MSI which are shown faded. SNO-HA confidence interval ±3σ.

Using a methodology based on SBAF applied to the PICS Algeria-3, Algeria-5, Egypt-1 and Libya-4. Barsi et al. [43] also compared S2A/B MSI with OLI. Continuing with the per-model comparison philosophy, we also added our results to the latest data published by Barsi et al. [44] in which they compared S2A/B MSI with OLI data (Figures 22 and 23).

Our methodology shows that S2A yields higher reflectance values than S2B for most of the studied bands. We attribute this effect to the small and systematic difference in radiometry of about 1% detected by ESA in the Sentinel-2 L1C Data Quality Report and which it is currently under study by the MPC [42]. This discrepancy has also been previously observed by other authors, such as Helder et al. [4].

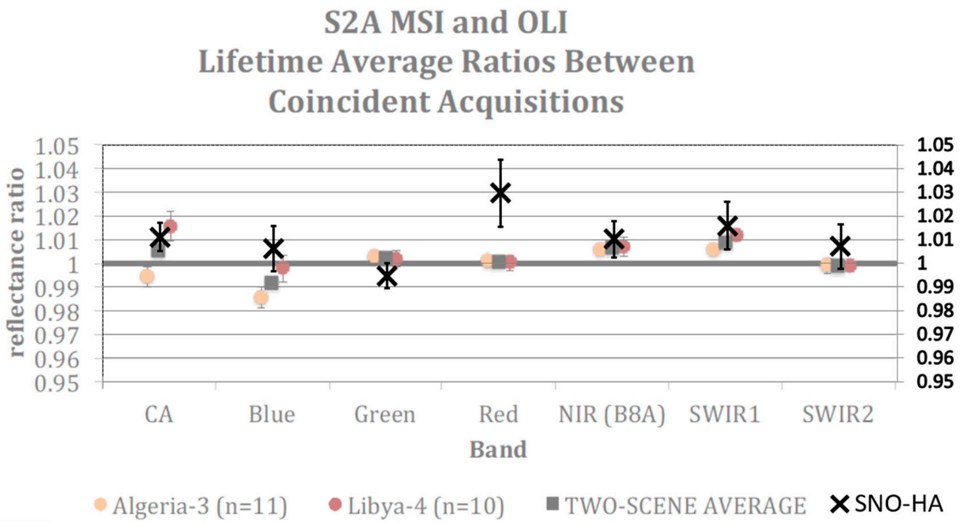

Figure 22. S2A vs. L8 slopes from Table 3 (SNO-HA method) solid black crosses over the results obtained on Algeria-3 and Libya-4 by Barsi et al. with S2A which are shown faded. SNO-HA confidence interval ±3σ.

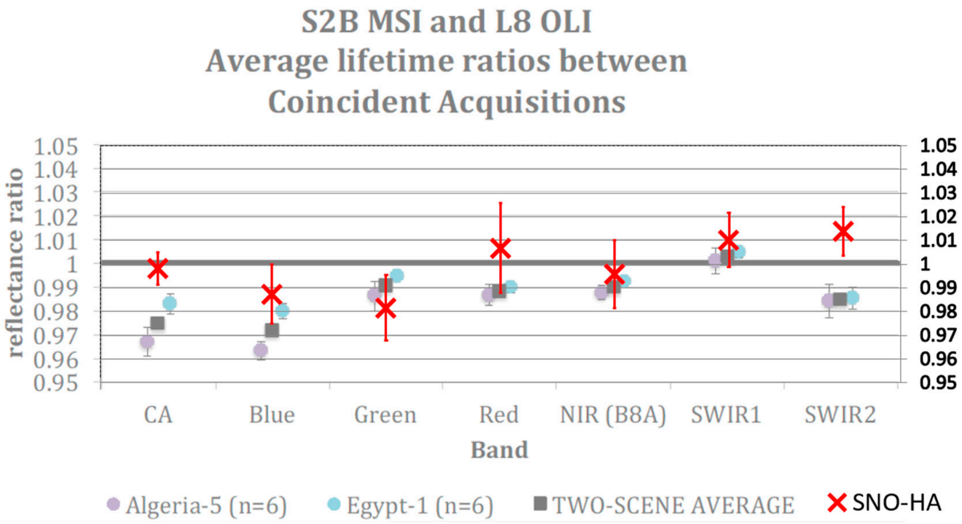

Figure 23. S2B vs. L8 slopes from Table 4 (SNO-HA method) red crosses over the results obtained on Algeria-5 and Egypt-1 by Barsi et al. with S2B which are shown faded. SNO-HA confidence interval ±3σ.

The wide NIR band shows the lowest coefficients of determination with the narrow NIR of L8, 0.980 and 0.984 for S2 A/B, respectively. The effect can also be observed as a large confidence interval in Figures 20 and 21. This is consistent with the fact that their RSRs are largely different. Apart from the wide NIR, the red band of S2A shows the largest deviation. For this reason, we chose this band to focus on the ground classes breakdown. Recalling that the ratios are inverted in Figure 18, we see that S2A yields higher values in all the represented classes, which is in agreement with the effect under study by the MPC [42]. We also observe that S2B ratios have larger variability across classes when compared with S2A.

The S2A/MSI and S2B/MSI are largely interoperable with L8/OLI for all studied bands with the exception of the wide NIR, which correlates notably worse. The slopes in Tables 3 and 4 are the corrective factors that account for the different responses of each band pair. The satellites S2A and S2B are orbiting in the same plane and maintained in a phase shift of 180° [26,28]. This creates a special case where the IATGs are always significatively longer than one day. For this reason, their interoperability cannot be directly studied using this methodology. It could be inferred from our results, but it falls outside the scope of this work.

This methodology could be applied to other polar sun-synchronous satellites with similar characteristics, such as GaoFen-6/WFC, PROBA-V, Deimos-1 [45,46], or the future SeoSat (Ingenio) [47], even if they are in opposed orbit directions. With our methodology, it is possible to implement semi-automated quality assessment and quality control procedures because there is no need for BRDF calculations or atmospheric correction. Apart from the outlier inspection, the rest of the processes can be automated, including metadata retrieval, ground trajectory determination, SNO identification, data download, HAs creation, statistics extraction and representation.

5. Conclusions

In this work, we propose an empirical sensor comparison methodology for all spectral targets, based on SNOs, which does not need BRDF modelling or atmospheric correction to yield robust results. Due to its empirical approach, model-based techniques like the Spectral Band Adjustment Factors (SBAF) and atmospheric corrections are avoided. With illumination, ground and atmospheric effects minimized, the differences between intrinsic sensor characteristics, RSRs included, appear naturally, encompassed as slopes and uncertainties. The global scope of the method allows the acquisition of diverse ground types, with different spectral signatures and wide TOA reflectance ranges. Hence, enabling the creation of heterogeneous datasets for comprehensive cross-calibration analysis. The ground classes distribution will cause the slopes to have a systematic error that diminishes as diversity grows in the data set.

This procedure was used to assess the interoperability of L8 with S2A and L8 with S2B. In both cases, the band correlation calculations yielded high coefficients of variation. Showing that they are largely interoperable, with the exception of the wide NIR band, for which a research path was hinted. The methodology consistency was reassured by comparison with the results provided by third-party methods.

The presented technique can be extended. Since the L8 and S2 orbit planes are very close so their orbits run almost parallel for long distances [48] the SNO intersection point could be redefined as a segment, allowing larger SNO datasets. MSI tiles can be seamlessly mosaicked, without resampling, when they are in the same projection creating a bigger sample. Moreover, the lack of correlation of the residuals with the HAs distance to nadir and IATG means that both can be increased. Note that the method behaved well even with strongly anisotropic BRDFs (Figure 14). The number of valid SNOs could also increase raising the maximum cloudiness threshold. Another possibility to explore would be the usability of cloudy SNOs with extremely short IATGs. We have found that even minor anomalies are salient in the regressions, therefore, it would be possible to replace the visual outlier removal process with an automated one.

SNOs and HAs calculations are simple when compared with BRDF and atmospheric corrections. Therefore, this empirical method can be seamlessly extended for the assessment of other sensors, being the ground trajectory determination is the only element needing customization.

Author Contributions: Author Contributions: Conceptualization, J.G. and J.F.R.; Methodology, J.G. and J.F.R.; Formal Analysis, J.G., J.F.R. and P.S.; Validation, J.G., J.F.R., P.S. and D.G.; Data Curation, J.G. and J.F.R.; Writing—Original Draft Preparation, J.G. and J.F.R.; Writing—Review and Editing, J.G., J.F.R., P.S., D.G., J.L.C. and J.S.; Supervision, J.G., J.F.R., P.S., D.G., J.S. and J.L.C.; Project Administration, J.S. All authors have read and agreed to the published version of the manuscript.

Funding: This research did not receive any specific grant from funding agencies in the public, commercial, or not-for-profit sectors.

Conflicts of Interest: All authors declare that they have no conflict of interest.

Appendix A

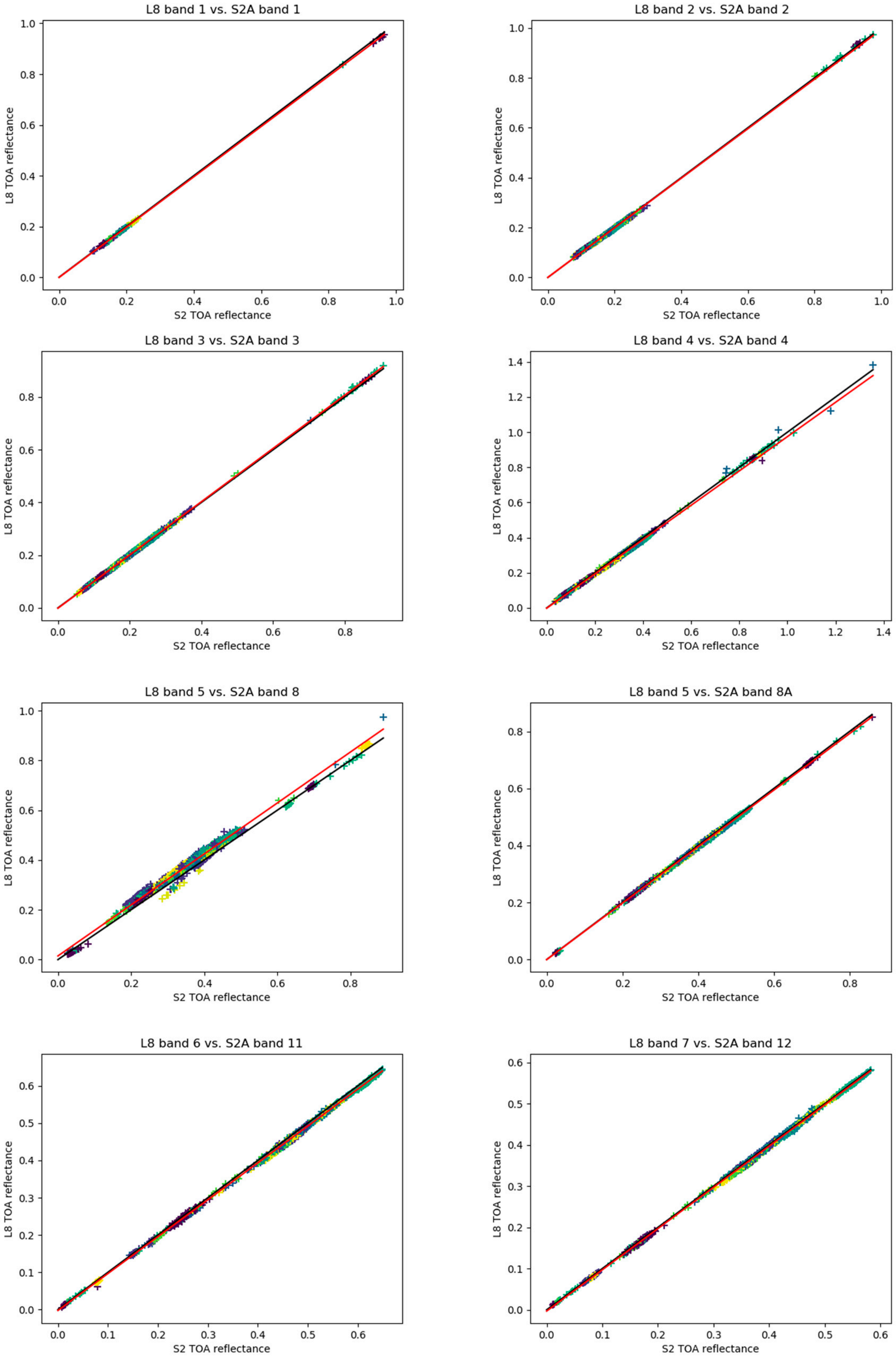

Figure A1. L8 vs. S2A linear regression plots. Each point is a different HA. Points with different colors belong to different SNOs. Red line is the linear regression.

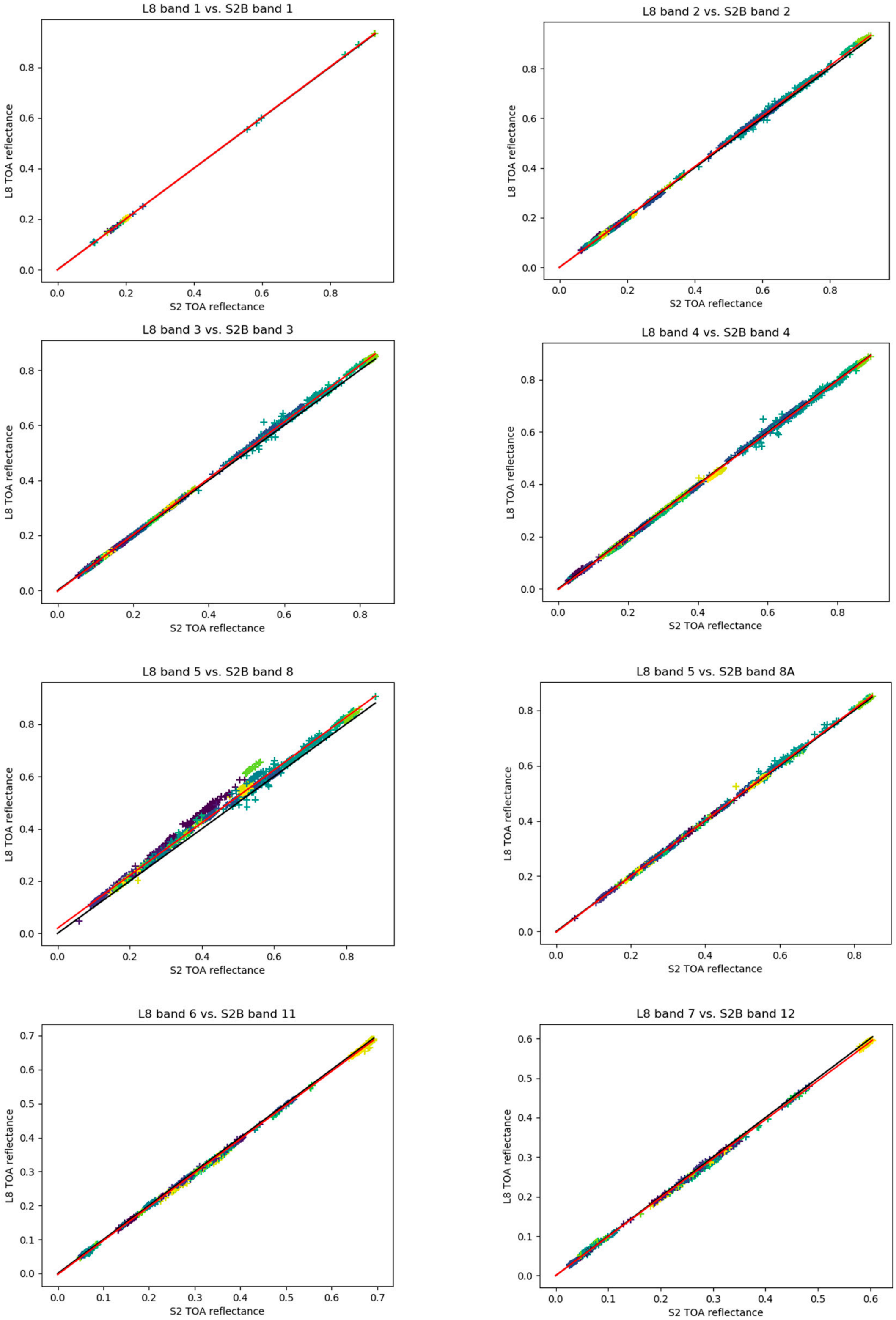

Figure A2. L8 vs. S2B linear regression plots. Each point is a different HA. Points with different colors belong to different SNOs. Red line is the linear regression.

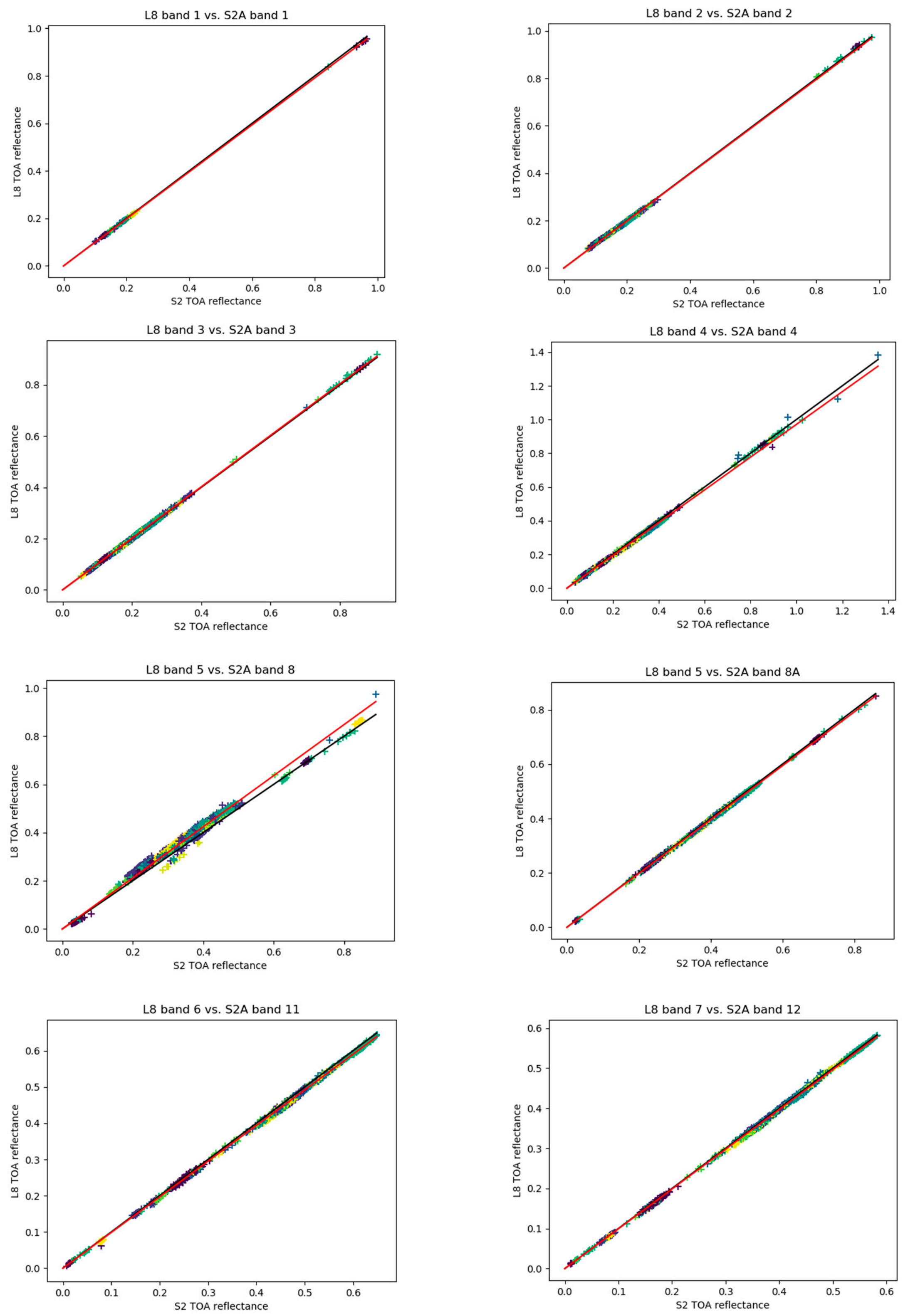

Figure A3. L8 vs. S2A zero-intercept plots. Each point is a different HA. Points with different colors belong to different SNOs. Red line is the calculated slope. Black is slope 1.

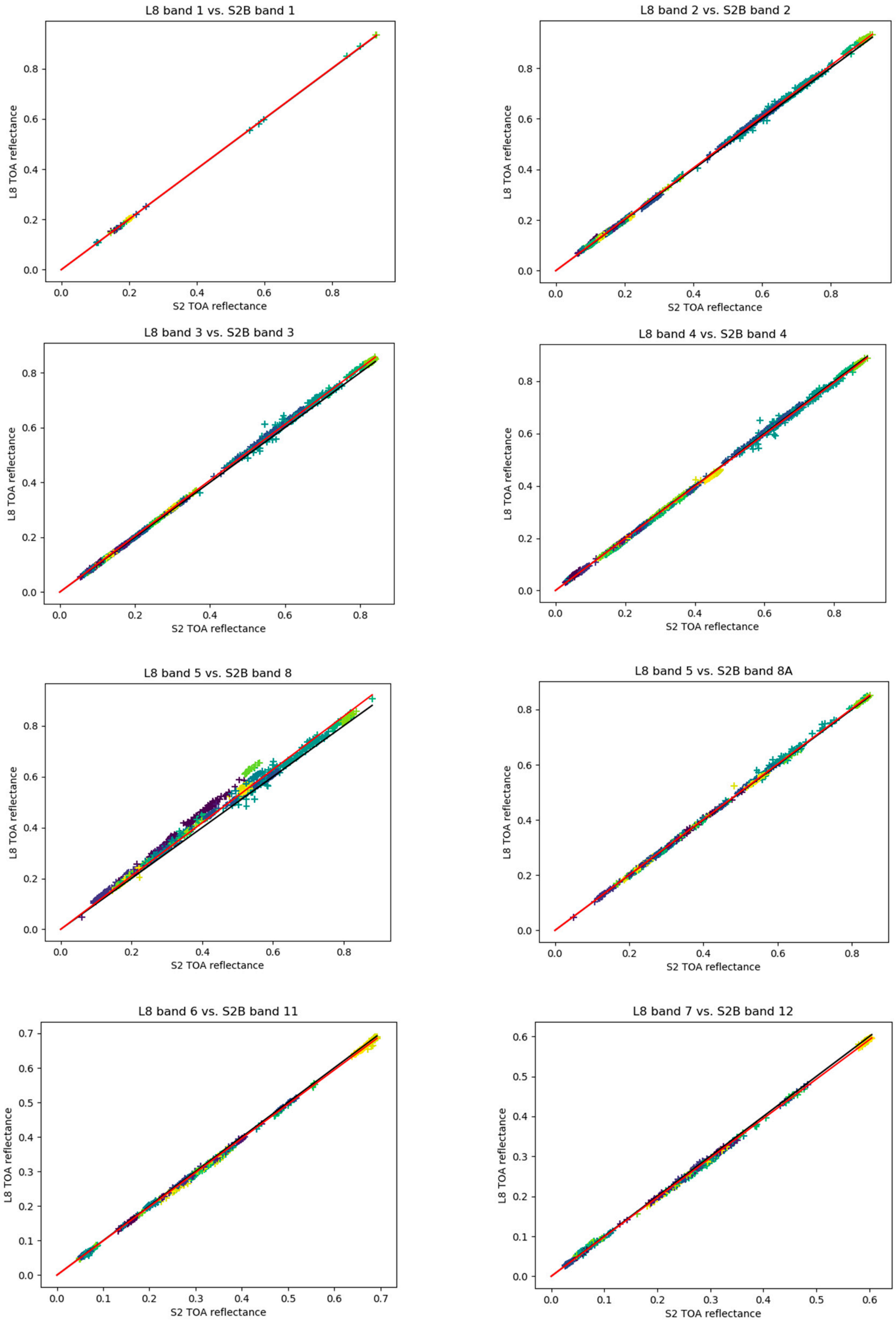

Figure A4. L8 vs. S2B zero-intercept plots. Each point is a different HA. Points with different colors belong to different SNOs. Red line is the calculated slope. Black is slope 1.

Appendix B

Table A1. SNOs after IATG and cloudiness filtering.

Acquisition Date	Sentinel Product Identifier	Landsat Product Identifier	SNO Intersection Lon, Lat (°)
2015-08-12	S2A_MSIL1C_20150812T104026_N0204_R008_T31TEJ_20150812T104021	LC08_L1TP_197030_20150812_20170406_01_T1	3.4687, 43.5385
2015-09-04	S2A_MSIL1C_20150904T072816_N0204_R049_T39UXP_20150904T073107	LC08_L1TP_166027_20150904_20170404_01_T1	52.9557, 47.8579
2015-11-15	S2A_MSIL1C_20151115T163532_N0204_R083_T16TGQ_20151115T163534	LC08_L1TP_021029_20151115_20170225_01_T1	−84.1691, 44.8334
2015-12-04	S2A_MSIL1C_20151204T170702_N0204_R069_T14RQU_20151204T171455	LC08_L1TP_026039_20151204_20170224_01_T1	−96.4111, 29.8870
2016-01-23	S2A_MSIL1C_20160123T052112_N0201_R062_T43QGC_20160123T052434	LC08_L1TP_145046_20160123_20170405_01_T1	77.3742, 20.3053
2016-02-07	S2A_MSIL1C_20160207T112012_N0201_R137_T29RMJ_20160207T112209	LC08_L1TP_202042_20160207_20170330_01_T1	−9.4531, 25.4921
2016-03-28	S2A_MSIL1C_20160328T060612_N0201_R134_T47XNE_20160328T060634	LC08_L1TP_152006_20160328_20170327_01_T1	102.5021, 75.9571
2016-04-23	S2A_MSIL1C_20160423T163322_N0201_R083_T16TFN_20160423T163610	LC08_L1TP_021030_20160423_20170223_01_T1	−84.9030, 42.8084
2016-05-05	S2A_MSIL1C_20160505T004712_N0202_R102_T54HTK_20160505T004953	LC08_L1TP_098082_20160505_20170325_01_T1	138.1499, −31.9755
2016-05-16	S2A_MSIL1C_20160516T145922_N0202_R125_T22WFU_20160516T150205	LC08_L1TP_006013_20160516_20170324_01_T1	−48.4028, 66.4414
2016-06-08	S2A_MSIL1C_20160608T101032_N0202_R022_T33UWV_20160608T101220	LC08_L1TP_192023_20160608_20170324_01_T1	15.4202, 53.8655
2016-06-23	S2A_MSIL1C_20160623T142012_N0204_R096_T26XMG_20160623T142007	LC08_L1TP_233008_20160623_20170323_01_T1	−28.0386, 73.2500
2016-06-27	S2A_MSIL1C_20160627T085602_N0204_R007_T33MWM_20160627T091503	LC08_L1TP_181066_20160627_20170323_01_T1	15.5755, −8.1661
2016-08-04	S2A_MSIL1C_20160804T145922_N0204_R125_T22WFU_20160804T145917	LC08_L1TP_006013_20160804_20170322_01_T1	−48.1918, 66.6366
2016-08-27	S2A_MSIL1C_20160827T101022_N0204_R022_T33UWV_20160827T101025	LC08_L1TP_192023_20160827_20170321_01_T1	15.2991, 53.6280
2016-09-04	S2A_MSIL1C_20160904T024542_N0204_R132_T53WNR_20160904T024545	LC08_L1TP_120012_20160904_20170321_01_T1	137.3442, 68.1469
2016-10-12	S2A_MSIL1C_20161012T004702_N0204_R102_T54JUR_20161012T004954	LC08_L1TP_098079_20161012_20170319_01_T1	139.5657, −26.7139
2016-11-15	S2A_MSIL1C_20161115T083222_N0204_R021_T35PNP_20161115T084140	LC08_L1TP_176051_20161115_20170318_01_T1	27.7421, 12.6077
2016-12-08	S2A_MSIL1C_20161208T052212_N0204_R062_T43QGC_20161208T052504	LC08_L1TP_145046_20161208_20170317_01_T1	77.2887, 19.9503
2016-12-08	S2A_MSIL1C_20161208T070252_N0204_R063_T41UNB_20161208T070254	LC08_L1TP_161021_20161208_20170317_01_T1	63.9491, 55.1862
2016-12-19	S2A_MSIL1C_20161219T163702_N0204_R083_T16TGQ_20161219T163834	LC08_L1TP_021029_20161219_20170218_01_T1	−84.3506, 44.3429
2017-01-07	S2A_MSIL1C_20170107T170701_N0204_R069_T14RQT_20170107T170831	LC08_L1TP_026040_20170107_20170218_01_T1	−96.6369, 29.0480
2017-02-07	S2A_MSIL1C_20170207T063021_N0204_R077_T43VEJ_20170207T063023	LC08_L1TP_156017_20170207_20170216_01_T1	75.5459, 61.5073
2017-02-11	S2A_MSIL1C_20170211T024831_N0204_R132_T53WNQ_20170211T024828	LC08_L1TP_120013_20170211_20170217_01_T1	136.3952, 67.3552
2017-03-13	S2A_MSIL1C_20170313T110831_N0204_R137_T29RMJ_20170313T111212	LC08_L1TP_202042_20170313_20170328_01_T1	−9.4439, 25.5280

Table A1. *Cont.*

Acquisition Date	Sentinel Product Identifier	Landsat Product Identifier	SNO Intersection Lon, Lat (°)
2017-03-28	S2A_MSIL1C_20170328T170301_N0204_R069_T14RQT_20170328T170619	LC08_L1TP_026040_20170328_20170414_01_T1	−96.5164, 29.4971
2017-04-05	S2A_MSIL1C_20170405T075611_N0204_R035_T37REQ_20170405T081035	LC08_L1TP_171038_20170405_20170414_01_T1	39.9037, 31.2414
2017-04-24	S2A_MSIL1C_20170424T082601_N0204_R021_T35PNP_20170424T083830	LC08_L1TP_176051_20170424_20170502_01_T1	27.6998, 12.4221
2017-05-13	S2A_MSIL1C_20170513T090021_N0205_R007_T33MWM_20170513T092026	LC08_L1TP_181065_20170513_20170525_01_T1	15.6498, −7.8332
2017-06-01	S2A_MSIL1C_20170601T110651_N0205_R137_T29RMJ_20170601T111225	LC08_L1TP_202042_20170601_20170615_01_T1	−9.3525, 25.8857
2017-06-09	S2A_MSIL1C_20170609T004711_N0205_R102_T54JUQ_20170609T005308	LC08_L1TP_098079_20170609_20170616_01_T1	139.3032, −27.7203
2017-06-24	S2A_MSIL1C_20170624T075611_N0205_R035_T37SFS_20170624T075954	LC08_L1TP_171037_20170624_20170701_01_T1	40.3766, 32.9272
2017-07-13	S2A_MSIL1C_20170713T150911_N0205_R025_T25XEF_20170713T150911	LC08_L1TP_007005_20170713_20170726_01_T1	−31.3113, 76.5751
2017-07-15	S2B_MSIL1C_20170715T081609_N0205_R121_T38VNL_20170715T081603	LC08_L1TP_174019_20170715_20170727_01_T1	46.2853, 59.3029
2017-07-28	S2A_MSIL1C_20170728T155901_N0205_R097_T22XDG_20170728T160023	LC08_L1TP_016008_20170728_20170810_01_T1	−52.9801, 73.3561
2017-08-01	S2A_MSIL1C_20170801T140021_N0205_R010_T26WNE_20170801T140016	LC08_L1TP_229009_20170801_20170811_01_T1	−25.5732, 71.9617
2017-08-14	S2B_MSIL1C_20170814T183309_N0205_R127_T11SPV_20170814T183307	LC08_L1TP_039035_20170814_20170825_01_T1	−114.9258, 35.6075
2017-08-20	S2A_MSIL1C_20170820T160901_N0205_R140_T22XDH_20170820T160902	LC08_L1TP_017007_20170820_20170826_01_T1	−53.0172, 74.4073
2017-08-20	S2A_MSIL1C_20170820T110651_N0205_R137_T29RMJ_20170820T111220	LC08_L1TP_202042_20170820_20170826_01_T1	−9.2816, 26.1619
2017-08-22	S2B_MSIL1C_20170822T141949_N0205_R096_T27XVD_20170822T141947	LC08_L1TP_232007_20170822_20170911_01_T1	−22.9999, 75.2631
2017-08-28	S2A_MSIL1C_20170828T004711_N0205_R102_T54JUR_20170828T005307	LC08_L1TP_098078_20170828_20170914_01_T1	139.6069, −26.5550
2017-09-04	S2A_MSIL1C_20170904T165851_N0205_R069_T14RQV_20170904T170402	LC08_L1TP_026039_20170904_20180125_01_T1	−96.1340, 30.9020
2017-09-10	S2B_MSIL1C_20170910T095019_N0205_R079_T32QNJ_20170910T100356	LC08_L1TP_189045_20170910_20170927_01_T1	9.5894, 21.0792
2017-09-12	S2A_MSIL1C_20170912T075611_N0205_R035_T37SFT_20170912T075950	LC08_L1TP_171037_20170912_20170928_01_T1	40.6307, 33.8132
2017-09-20	S2A_MSIL1C_20170920T021601_N0205_R003_T55WEU_20170920T021627	LC08_L1TP_115010_20170920_20170930_01_T1	148.6628, 70.8084
2017-09-25	S2B_MSIL1C_20170925T142029_N0205_R010_T20JKN_20170925T142023	LC08_L1TP_230081_20170925_20180528_01_T1	−65.1780, −29.8396
2017-10-20	S2A_MSIL1C_20171020T090021_N0205_R007_T33LVH_20171020T091816	LC08_L1TP_181068_20171020_20171106_01_T1	14.9176, −11.0946
2017-10-22	S2B_MSIL1C_20171022T071249_N0205_R106_T38NPK_20171022T072130	LC08_L1TP_163057_20171022_20171107_01_T1	45.9595, 4.0151
2017-11-08	S2A_MSIL1C_20171108T111251_N0206_R137_T29QMG_20171108T145151	LC08_L1TP_202043_20171108_20171121_01_T1	−9.8014, 24.1148
2017-11-29	S2B_MSIL1C_20171129T095339_N0206_R079_T32QNJ_20171129T115638	LC08_L1TP_189046_20171129_20171207_01_T1	9.5698, 20.9984
2017-11-29	S2B_MSIL1C_20171129T113419_N0206_R080_T30UVG_20171129T133534	LC08_L1TP_205021_20171129_20171207_01_T1	−3.7183, 55.7397
2017-11-29	S2B_MSIL1C_20171129T081249_N0206_R078_T34HFK_20171129T115343	LC08_L1TP_173082_20171129_20171207_01_T1	22.2712, −32.2408
2017-12-01	S2A_MSIL1C_20171201T080301_N0206_R035_T37SFS_20171201T100357	LC08_L1TP_171037_20171201_20171207_01_T1	40.4777, 33.2813

Table A1. *Cont.*

Acquisition Date	Sentinel Product Identifier	Landsat Product Identifier	SNO Intersection Lon, Lat (°)
2018-01-27	S2A_MSIL1C_20180127T111321_N0206_R137_T29RMK_20180127T162747	LC08_L1TP_202042_20180127_20180207_01_T1	−9.1689, 26.5989
2018-01-29	S2B_MSIL1C_20180129T092229_N0206_R093_T34SEH_20180129T112249	LC08_L1TP_184034_20180129_20180207_01_T1	21.7305, 37.9342
2018-02-17	S2B_MSIL1C_20180217T081009_N0206_R078_T34JFL_20180217T121107	LC08_L1TP_173082_20180217_20180307_01_T1	22.5676, −31.1783
2018-03-04	S2B_MSIL1C_20180304T142029_N0206_R010_T20JLR_20180304T191354	LC08_L1TP_230079_20180304_20180319_01_T1	−64.3401, −26.6743
2018-03-10	S2A_MSIL1C_20180310T082751_N0206_R021_T35PPS_20180310T122012	LC08_L1TP_176050_20180310_20180320_01_T1	28.2813, 14.9583
2018-03-12	S2B_MSIL1C_20180312T063639_N0206_R120_T40RGR_20180312T102023	LC08_L1TP_158041_20180312_20180320_01_T1	59.1391, 27.8870
2018-03-31	S2B_MSIL1C_20180331T070619_N0206_R106_T38NPP_20180331T100829	LC08_L1TP_163055_20180331_20180405_01_T1	46.7244, 7.4643
2018-04-02	S2A_MSIL1C_20180402T051651_N0206_R062_T43QGD_20180402T090406	LC08_L1TP_145046_20180402_20180416_01_T1	77.5245, 20.9270
2018-04-11	S2B_MSIL1C_20180411T181919_N0206_R127_T11SPT_20180411T220513	LC08_L1TP_039036_20180411_20180417_01_T1	−115.3518, 34.1632
2018-04-17	S2A_MSIL1C_20180417T110651_N0206_R137_T29RMH_20180417T164957	LC08_L1TP_202043_20180417_20180501_01_T1	−9.5650, 25.0522
2018-04-25	S2A_MSIL1C_20180425T004711_N0206_R102_T54JUT_20180425T021141	LC08_L1TP_098077_20180425_20180502_01_T1	140.0578, −24.7916
2018-05-08	S2B_MSIL1C_20180508T080609_N0206_R078_T34HFK_20180508T133204	LC08_L1TP_173082_20180508_20180517_01_T1	22.2174, −32.4317
2018-05-10	S2A_MSIL1C_20180510T094031_N0206_R036_T35VME_20180510T114819	LC08_L1TP_187019_20180510_20180517_01_T1	25.3924, 58.1392
2018-05-10	S2A_MSIL1C_20180510T043701_N0206_R033_T50XNG_20180510T074003	LC08_L1TP_139008_20180510_20180517_01_T1	117.6388, 73.0903
2018-05-12	S2B_MSIL1C_20180512T074729_N0206_R135_T40VDP_20180512T113937	LC08_L1TP_169017_20180512_20180517_01_T1	55.7179, 61.9131
2018-05-16	S2B_MSIL1C_20180516T022549_N0206_R046_T52UFE_20180516T040424	LC08_L1TP_117022_20180516_20180604_01_T1	131.2951, 54.0036
2018-05-16	S2B_MSIL1C_20180516T040539_N0206_R047_T50WMV_20180516T070218	LC08_L1TP_133013_20180516_20180604_01_T1	116.1178, 67.2360
2018-05-23	S2B_MSIL1C_20180523T142039_N0206_R010_T20JLP_20180523T192205	LC08_L1TP_230080_20180523_20180605_01_T1	−64.8003, −28.4302
2018-05-23	S2B_MSIL1C_20180523T204019_N0206_R014_T10XDG_20180524T001026	LC08_L1TP_061008_20180523_20180605_01_T1	−123.9418, 73.1388
2018-06-04	S2B_MSIL1C_20180604T043659_N0206_R033_T48WXU_20180604T081821	LC08_L1TP_138013_20180604_20180615_01_T1	107.7603, 66.5143
2018-06-06	S2A_MSIL1C_20180606T024651_N0206_R132_T53WPS_20180606T040212	LC08_L1TP_120011_20180606_20180615_01_T1	138.5057, 69.0425
2018-06-07	S2B_MSIL1C_20180607T180919_N0206_R084_T17XMD_20180607T213729	LC08_L1TP_038006_20180607_20180615_01_T1	−80.8364, 75.2836
2018-06-11	S2B_MSIL1C_20180611T174909_N0206_R141_T13UFR_20180611T213053	LC08_L1TP_034025_20180611_20180615_01_T1	−102.1482, 50.1601
2018-06-13	S2A_MSIL1C_20180613T155901_N0206_R097_T19VCC_20180613T194300	LC08_L1TP_016021_20180613_20180703_01_T1	−71.3207, 56.3924
2018-06-23	S2B_MSIL1C_20180623T020449_N0206_R017_T51KTT_20180623T033510	LC08_L1TP_111074_20180623_20180703_01_T1	120.9584, −20.5823
2018-06-30	S2B_MSIL1C_20180630T181919_N0206_R127_T11SQA_20180630T232219	LC08_L1TP_039035_20180630_20180716_01_T1	−114.5805, 36.7495
2018-07-02	S2A_MSIL1C_20180702T150721_N0206_R082_T19MBT_20180702T195445	LC08_L1TP_005062_20180702_20180716_01_T1	−71.3037, −2.6055
2018-07-02	S2A_MSIL1C_20180702T162901_N0206_R083_T16TGS_20180702T214026	LC08_L1TP_021028_20180702_20180716_01_T1	−83.6504, 46.1967

Table A1. *Cont.*

Acquisition Date	Sentinel Product Identifier	Landsat Product Identifier	SNO Intersection Lon, Lat (°)
2018-07-10	S2A_MSIL1C_20180710T072621_N0206_R049_T39UXP_20180710T085441	LC08_L1TP_166027_20180710_20180717_01_T1	53.0450, 48.0755
2018-07-12	S2B_MSIL1C_20180712T053639_N0206_R005_T44UPF_20180712T092034	LC08_L1TP_148022_20180712_20180717_01_T1	83.8405, 54.7237
2018-07-14	S2A_MSIL1C_20180714T004711_N0206_R102_T54JUR_20180714T021605	LC08_L1TP_098078_20180714_20180730_01_T1	139.6443, −26.4100
2018-07-27	S2B_MSIL1C_20180727T095029_N0206_R079_T32QNK_20180727T135801	LC08_L1TP_189045_20180727_20180731_01_T1	9.8901, 22.3097
2018-07-29	S2A_MSIL1C_20180729T075611_N0206_R035_T37SFU_20180729T092130	LC08_L1TP_171036_20180729_20180813_01_T1	40.9243, 34.8195
2018-07-29	S2A_MSIL1C_20180729T094031_N0206_R036_T35VNJ_20180729T101505	LC08_L1TP_187017_20180729_20180813_01_T1	27.7539, 61.5600
2018-07-31	S2B_MSIL1C_20180731T060629_N0206_R134_T42TYQ_20180731T084741	LC08_L1TP_153029_20180731_20180814_01_T1	71.8012, 44.5272
2018-08-11	S2B_MSIL1C_20180811T142029_N0206_R010_T20JKN_20180811T194747	LC08_L1TP_230081_20180811_20180815_01_T1	−65.0898, −29.5130
2018-08-19	S2B_MSIL1C_20180819T063619_N0206_R120_T40RGS_20180819T093637	LC08_L1TP_158040_20180819_20180829_01_T1	59.2724, 28.3919
2018-08-21	S2A_MSIL1C_20180821T044701_N0206_R076_T45TYE_20180821T075342	LC08_L1TP_140033_20180821_20180829_01_T1	90.2648, 39.6924
2018-09-07	S2B_MSIL1C_20180907T070609_N0206_R106_T38NPP_20180907T110607	LC08_L1TP_163055_20180907_20180912_01_T1	46.8043, 7.8230
2018-09-11	S2B_MSIL1C_20180911T020439_N0206_R017_T51KUU_20180911T052025	LC08_L1TP_111074_20180911_20180927_01_T1	121.1695, −19.7059
2018-09-11	S2B_MSIL1C_20180911T032529_N0206_R018_T49SCU_20180911T070657	LC08_L1TP_127036_20180911_20180927_01_T1	108.9604, 35.0366
2018-09-13	S2A_MSIL1C_20180913T031541_N0206_R118_T51WXN_20180913T051046	LC08_L1TP_125015_20180913_20180927_01_T1	126.3121, 64.9526
2018-09-18	S2B_MSIL1C_20180918T182009_N0206_R127_T11SQB_20180918T221717	LC08_L1TP_039034_20180918_20180928_01_T1	−114.4716, 37.1044
2018-09-20	S2A_MSIL1C_20180920T150721_N0206_R082_T19MBU_20180920T184627	LC08_L1TP_005061_20180920_20180928_01_T1	−71.0166, −1.3029
2018-09-24	S2A_MSIL1C_20180924T110801_N0206_R137_T29RNL_20180924T152333	LC08_L1TP_202041_20180924_20180929_01_T1	−8.9195, 27.5574
2018-09-26	S2B_MSIL1C_20180926T073639_N0206_R092_T36LXK_20180926T113524	LC08_L1TP_168070_20180926_20181009_01_T1	34.2997, −14.4166
2018-09-28	S2A_MSIL1C_20180928T072651_N0206_R049_T39TXN_20180928T141734	LC08_L1TP_166027_20180928_20181009_01_T1	52.7750, 47.4132
2018-09-30	S2B_MSIL1C_20180930T053639_N0206_R005_T44UPE_20180930T092159	LC08_L1TP_148022_20180930_20181010_01_T1	83.4770, 54.0308
2018-10-02	S2A_MSIL1C_20181002T004701_N0206_R102_T54JUR_20181002T022020	LC08_L1TP_098078_20181002_20181010_01_T1	139.6300, −26.4656
2018-10-09	S2A_MSIL1C_20181009T184251_N0206_R070_T12VWM_20181009T222044	LC08_L1TP_042018_20181009_20181029_01_T1	−109.5548, 59.6649
2018-10-11	S2B_MSIL1C_20181011T135109_N0206_R024_T22LBP_20181011T172553	LC08_L1TP_225067_20181011_20181030_01_T1	−52.9522, −10.6420
2018-10-15	S2B_MSIL1C_20181015T113319_N0206_R080_T30UVG_20181015T133405	LC08_L1TP_205021_20181015_20181030_01_T1	−3.7972, 55.5972
2018-11-05	S2A_MSIL1C_20181105T083121_N0206_R021_T35PNP_20181105T100715	LC08_L1TP_176052_20181105_20181115_01_T1	27.5869, 11.9251
2018-11-07	S2B_MSIL1C_20181107T064049_N0207_R120_T40RFP_20181107T103500	LC08_L1TP_158042_20181107_20181116_01_T1	58.6302, 25.9275
2018-11-09	S2A_MSIL1C_20181109T063051_N0207_R077_T43VEJ_20181109T083632	LC08_L1TP_156017_20181109_20181116_01_T1	75.9871, 62.0783
2018-11-11	S2B_MSIL1C_20181111T025939_N0207_R032_T50TQS_20181111T055543	LC08_L1TP_122028_20181111_20181127_01_T1	120.4116, 46.5705

Table A1. *Cont.*

Acquisition Date	Sentinel Product Identifier	Landsat Product Identifier	SNO Intersection Lon, Lat (°)
2018-11-28	S2A_MSIL1C_20181128T052141_N0207_R062_T43QGD_20181128T090704	LC08_L1TP_145046_20181128_20181211_01_T1	77.4906, 20.7869
2018-11-30	S2B_MSIL1C_20181130T020439_N0207_R017_T51KTT_20181130T060546	LC08_L1TP_111074_20181130_20181211_01_T1	120.9916, −20.4450
2018-12-28	S2A_MSIL1C_20181228T170711_N0207_R069_T14RQV_20181228T202923	LC08_L1TP_026039_20181228_20190129_01_T1	−96.0964, 31.0386
2019-01-03	S2B_MSIL1C_20190103T095409_N0207_R079_T32QNJ_20190103T115034	LC08_L1TP_189045_20190103_20190130_01_T1	9.6094, 21.1616
2019-01-03	S2B_MSIL1C_20190103T081329_N0207_R078_T34HFK_20190103T102420	LC08_L1TP_173082_20190103_20190130_01_T1	22.2585, −32.2861
2019-01-24	S2A_MSIL1C_20190124T083231_N0207_R021_T35PPT_20190124T095836	LC08_L1TP_176049_20190124_20190205_01_T1	28.4836, 15.8312
2019-01-28	S2A_MSIL1C_20190128T063121_N0207_R077_T43VEK_20190128T075200	LC08_L1TP_156016_20190128_20190206_01_T1	76.2697, 62.4334
2019-02-14	S2B_MSIL1C_20190214T071009_N0207_R106_T38PQQ_20190214T104949	LC08_L1TP_163054_20190214_20190222_01_T1	47.0368, 8.8635
2019-02-20	S2A_MSIL1C_20190220T031751_N0207_R118_T51VXL_20190220T050828	LC08_L1TP_125015_20190220_20190222_01_T1	125.3264, 63.8829
2019-03-03	S2A_MSIL1C_20190303T110951_N0207_R137_T29RML_20190303T132419	LC08_L1TP_202041_20190303_20190309_01_T1	−9.0120, 27.2033
2019-03-11	S2A_MSIL1C_20190311T004701_N0207_R102_T54KVV_20190311T022013	LC08_L1TP_098076_20190311_20190325_01_T1	140.4117, −23.3815
2019-04-08	S2B_MSIL1C_20190408T142039_N0207_R010_T20JLP_20190408T174012	LC08_L1TP_230080_20190408_20190422_01_T1	−64.7462, −28.2261
2019-05-05	S2B_MSIL1C_20190505T084609_N0207_R107_T36UWB_20190505T111007	LC08_L1TP_179025_20190505_20190520_01_T1	34.1044, 50.8476
2019-05-07	S2A_MSIL1C_20190507T051651_N0207_R062_T43QGD_20190507T085455	LC08_L1TP_145045_20190507_20190521_01_T1	77.6001, 21.2382
2019-05-22	S2A_MSIL1C_20190522T160911_N0207_R140_T22XDH_20190522T212646	LC08_L1TP_017007_20190522_20190604_01_T1	−52.6242, 74.5578
2019-05-22	S2A_MSIL1C_20190522T110621_N0207_R137_T29RMH_20190522T181102	LC08_L1TP_202043_20190522_20190604_01_T1	−9.5346, 25.1720
2019-05-30	S2A_MSIL1C_20190530T004711_N0207_R102_T54JUP_20190530T022148	LC08_L1TP_098080_20190530_20190605_01_T1	139.0652, −28.6207
2019-06-06	S2A_MSIL1C_20190606T165901_N0207_R069_T14RQT_20190606T220932	LC08_L1TP_026040_20190606_20190619_01_T1	−96.5873, 29.2330
2019-06-08	S2B_MSIL1C_20190608T215539_N0207_R029_T06WVC_20190608T233549	LC08_L1TP_072011_20190608_20190619_01_T1	−147.4049, 69.8160
2019-06-12	S2B_MSIL1C_20190612T095039_N0207_R079_T32QMF_20190612T120554	LC08_L1TP_189047_20190612_20190619_01_T1	9.0059, 18.6496
2019-06-14	S2A_MSIL1C_20190614T075611_N0207_R035_T37SER_20190614T092644	LC08_L1TP_171038_20190614_20190620_01_T1	40.0994, 31.9447
2019-06-22	S2A_MSIL1C_20190622T053651_N0207_R005_T48XVG_20190622T073519	LC08_L1TP_147008_20190622_20190704_01_T1	103.8639, 73.6931
2019-06-25	S2A_MSIL1C_20190625T141011_N0207_R053_T26XNG_20190625T142549	LC08_L1TP_232008_20190625_20190705_01_T1	−26.0279, 73.0120
2019-06-27	S2B_MSIL1C_20190627T142049_N0207_R010_T20JKL_20190627T173831	LC08_L1TP_230081_20190627_20190705_01_T1	−65.4539, −30.8507
2019-07-05	S2B_MSIL1C_20190705T063639_N0207_R120_T40RFR_20190705T092912	LC08_L1TP_158041_20190705_20190719_01_T1	59.0271, 27.4600
2019-07-07	S2A_MSIL1C_20190707T044711_N0207_R076_T45SYD_20190707T074645	LC08_L1TP_140033_20190707_20190719_01_T1	90.0519, 39.0348
2019-07-10	S2A_MSIL1C_20190710T214541_N0208_R129_T06WWB_20190710T232820	LC08_L1TP_072011_20190710_20190719_01_T1	−146.1640, 68.8994

Table A1. *Cont.*

Acquisition Date	Sentinel Product Identifier	Landsat Product Identifier	SNO Intersection Lon, Lat (°)
2019-07-18	S2A_MSIL1C_20190718T155911_N0208_R097_T19VCC_20190718T194134	LC08_L1TP_016021_20190718_20190731_01_T1	−71.5169, 56.0478
2019-07-20	S2B_MSIL1C_20190720T054649_N0208_R048_T47XNA_20190720T092848	LC08_L1TP_151008_20190720_20190731_01_T1	99.4777, 72.8331
2019-07-22	S2A_MSIL1C_20190722T104031_N0208_R008_T31TEJ_20190722T110458	LC08_L1TP_197030_20190722_20190801_01_T1	3.4531, 43.4949
2019-07-28	S2B_MSIL1C_20190728T020459_N0208_R017_T51KUU_20190728T051808	LC08_L1TP_111074_20190728_20190801_01_T1	121.1611, −19.7412
2019-07-30	S2A_MSIL1C_20190730T063631_N0208_R120_T46XEK_20190730T075058	LC08_L1TP_157006_20190730_20190801_01_T1	94.6434, 75.8645
2019-07-30	S2A_MSIL1C_20190730T031541_N0208_R118_T51WXN_20190730T050828	LC08_L1TP_125015_20190730_20190801_01_T1	126.3051, 64.9453
2019-07-30	S2A_MSIL1C_20190730T063631_N0208_R120_T45XWB_20190730T075058	LC08_L1TP_157008_20190730_20190801_01_T1	88.5970, 73.6222
2019-08-01	S2B_MSIL1C_20190801T030549_N0208_R075_T54XWG_20190801T045652	LC08_L1TP_123008_20190801_20190819_01_T1	141.2919, 73.5465
2019-08-06	S2A_MSIL1C_20190806T150721_N0208_R082_T19MBT_20190806T182907	LC08_L1TP_005062_20190806_20190820_01_T1	−71.1872, −2.0768
2019-08-10	S2A_MSIL1C_20190810T160911_N0208_R140_T22XDH_20190810T193101	LC08_L1TP_017007_20190810_20190820_01_T1	−52.5442, 74.5882
2019-08-12	S2B_MSIL1C_20190812T092039_N0208_R093_T34SEH_20190812T113125	LC08_L1TP_184033_20190812_20190820_01_T1	21.9898, 38.7538
2019-08-14	S2A_MSIL1C_20190814T072621_N0208_R049_T39TXN_20190814T084311	LC08_L1TP_166027_20190814_20190820_01_T1	52.8605, 47.6248
2019-08-18	S2A_MSIL1C_20190818T004711_N0208_R102_T54JUS_20190818T021956	LC08_L1TP_098078_20190818_20190902_01_T1	139.7911, −25.8391
2019-08-18	S2A_MSIL1C_20190818T052651_N0208_R105_T47WNT_20190818T083140	LC08_L1TP_146011_20190818_20190902_01_T1	99.9548, 70.2496
2019-08-31	S2B_MSIL1C_20190831T095039_N0208_R079_T32QNJ_20190831T133329	LC08_L1TP_189045_20190831_20190916_01_T1	9.7013, 21.5386
2019-09-02	S2A_MSIL1C_20190902T075611_N0208_R035_T37SFT_20190902T100157	LC08_L1TP_171036_20190902_20190916_01_T1	40.7337, 34.1685
2019-09-23	S2B_MSIL1C_20190923T063629_N0208_R120_T40RFR_20190923T103632	LC08_L1TP_158041_20190923_20190926_01_T1	59.0156, 27.4162
2019-09-27	S2B_MSIL1C_20190927T043659_N0208_R033_T48WWT_20190927T072914	LC08_L1TP_138014_20190927_20191017_01_T1	106.7168, 65.5093
2019-10-16	S2B_MSIL1C_20191016T020019_N0208_R017_T51KTS_20191016T051826	LC08_L1TP_111075_20191016_20191029_01_T1	120.8903, −20.8636
2019-10-23	S2B_MSIL1C_20191023T182419_N0208_R127_T11SPU_20191023T215755	LC08_L1TP_039036_20191023_20191030_01_T1	−115.1180, 34.9605

Appendix C

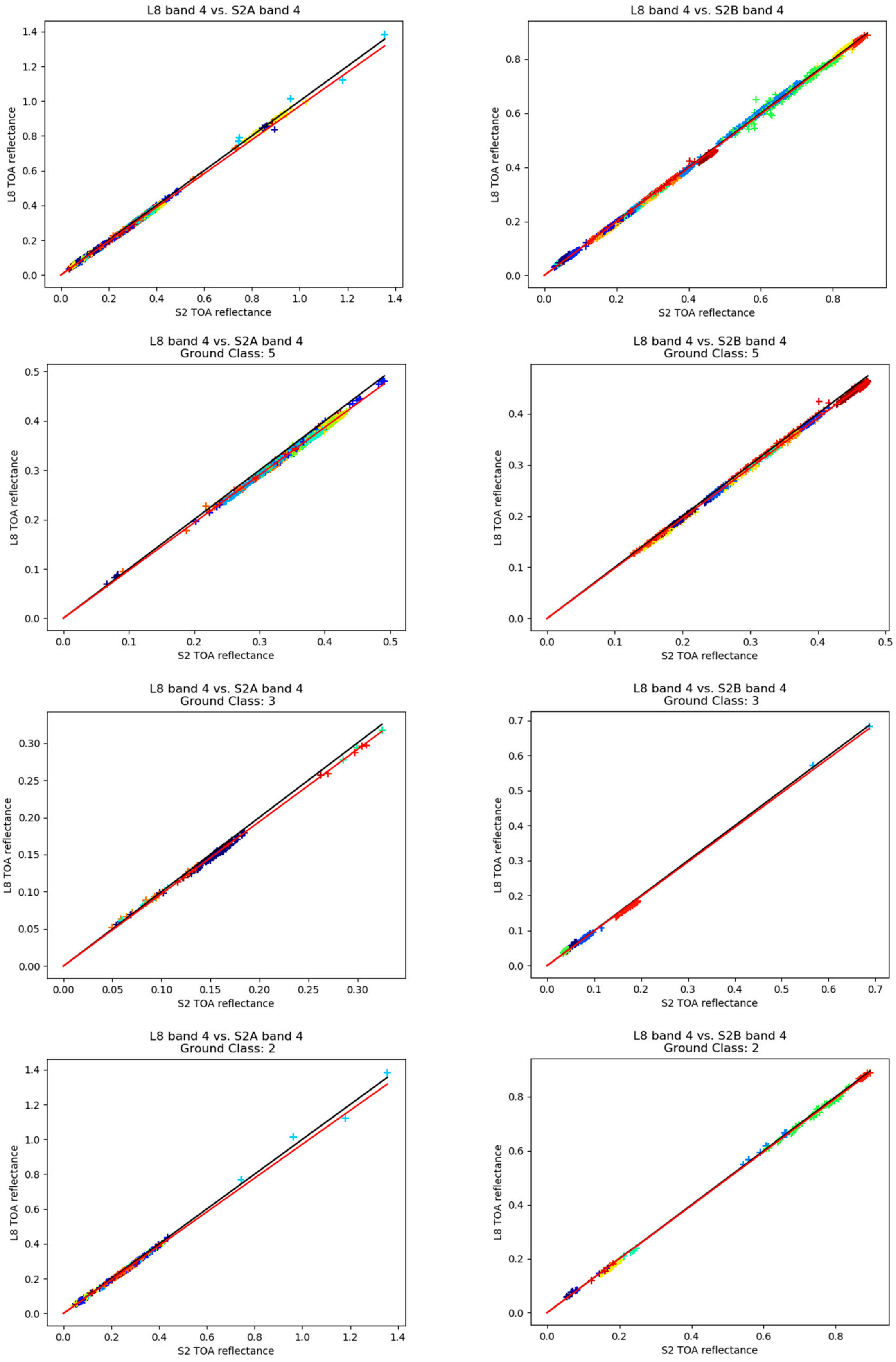
L8 band 4 vs. S2A band 4

L8 band 4 vs. S2B band 4

L8 band 4 vs. S2A band 4
Ground Class: 5

L8 band 4 vs. S2B band 4
Ground Class: 5

L8 band 4 vs. S2A band 4
Ground Class: 3

L8 band 4 vs. S2B band 4
Ground Class: 3

L8 band 4 vs. S2A band 4
Ground Class: 2

L8 band 4 vs. S2B band 4
Ground Class: 2

Figure A5. *Cont.*

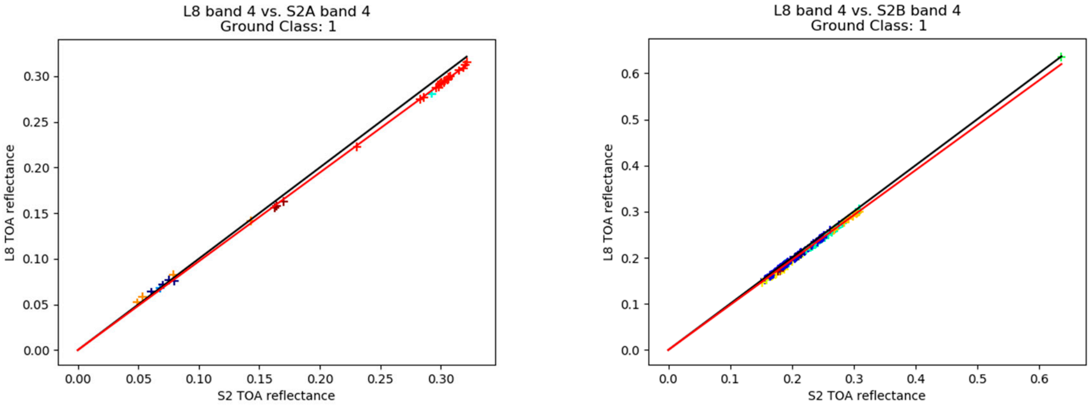

Figure A5. Linear regressions of MSI band 4 and OLI band 4 (red) for the most frequent classes. Each point is a different HA. Points with different colors belong to different SNOs. Red line is the linear regression. Black line is slope 1.

References

1. NOAA. Advisory Committee on Commercial Remote Sensing (ACCRES). Available online: https://www.nesdis.noaa.gov/CRSRA/pdf/AACRES_meeting_2018_Euroconsult.pdf (accessed on 15 February 2020).
2. Vescovi, F.D.; Lankester, T.; Coleman, E.; Ottavianelli, G. Harmonisation initiatives of Copernicus data quality control. In Proceedings of the International Archives of the Photogrammetry, Remote Sensing and Spatial Information Sciences, 2015 36th International Symposium on Remote Sensing of Environment, Berlin, Germany, 11–15 May 2015; Volume XL-7/W3.
3. Tansock, J.; Bancroft, D.; Butler, J.; Cao, C.; Datla, R.; Hansen, S.; Helder, D.; Kacker, R.; Latvakoski, H.; Mylnczak, M.; et al. *Guidelines for Radiometric Calibration of Electro-Optical Instruments for Remote Sensing*; Space Dynamics Lab Publications: Logan, UT, USA, 2015.
4. Helder, D.; Markham, B.; Morfitt, R.; Storey, J.; Barsi, J.; Gascon, F.; Clerc, S.; LaFrance, B.; Masek, J.; Roy, D.P.; et al. Observations and Recommendations for the Calibration of Landsat 8 OLI and Sentinel 2 MSI for Improved Data Interoperability. *Remote Sens.* **2018**, *10*, 1340. [CrossRef]
5. Müller, R. Calibration and verification of remote sensing instruments and observations. *Remote Sens.* **2014**, *6*, 5692–5695. [CrossRef]
6. Mishra, N.; Haque, M.O.; Leigh, L.; Aaron, D.; Helder, D.; Markham, B. Radiometric cross calibration of Landsat 8 operational land imager (OLI) and Landsat 7 enhanced thematic mapper plus (ETM+). *Remote Sens.* **2014**, *6*, 12619–12638. [CrossRef]
7. Mishra, N.; Helder, D.; Angal, A.; Choi, J.; Xiong, X. Absolute calibration of optical satellite sensors using Libya 4 pseudo invariant calibration site. *Remote Sens.* **2014**, *6*, 1327–1346. [CrossRef]
8. Helder, D.; Thome, K.J.; Mishra, N.; Chander, G.; Xiaoxiong, X.; Angal, A.; Taeyoung, C. Absolute Radiometric Calibration of Landsat Using a Pseudo Invariant Calibration Site. *IEEE Trans. Geosci. Remote Sens.* **2013**, *51*, 1360–1369. [CrossRef]
9. Bacour, C.; Briottet, X.; Bréon, F.M.; Viallefont-Robinet, F.; Bouvet, M. Revisiting Pseudo Invariant Calibration Sites (PICS) over sand deserts for vicarious calibration of optical imagers at 20 km and 100 km scales. *Remote Sens.* **2019**, *11*, 1166. [CrossRef]
10. Cook, M.; Padula, F.; Schott, J.; Cao, C. *Spatial, Spectral, and Radiometric Characterization of Libyan and Sonoran Desert Calibration Sites in Support of GOES-R Vicarious Calibration*; Rochester Institute of Technology, College of Science, Center for Imaging Science: Rochester, NY, USA, 2010.
11. Chander, G.; Mishra, N.; Helder, D.L.; Aaron, D.B.; Amit, A.; Choi, T.; Doelling, D.R. Applications of Spectral Band Adjustment Factors (SBAF) for cross-calibration. *IEEE Trans. Geosci. Remote Sens.* **2013**, *51*, 1267–1281. [CrossRef]
12. Chander, G.; Xiong, X.J.; Choi, T.J.; Angal, A. Monitoring on-orbit calibration stability of the Terra MODIS and Landsat 7 ETM+ sensors using pseudo-invariant test sites. *Remote Sens. Environ.* **2010**, *114*, 925–939. [CrossRef]

13. Chu, M.; Dodd, J. Ushering in the New Era of Radiometric Intercomparison of Multispectral Sensors with Precision SNO Analysis. *Climate* **2019**, *7*, 81. [CrossRef]
14. Uprety, S.; Cao, C.; Xiong, X.; Blonski, S.; Wu, A.; Shao, X. Radiometric intercomparison between Suomi-NPPVIIRS and AquaMODIS reflective solar bands using simultaneous nadir overpass in the low latitudes. *J. Atmos. Ocean. Technol.* **2013**, *30*, 2720–2736. [CrossRef]
15. Barrientos, C.; Mattar, C.; Nakos, T.; Perez, W. Radiometric cross-calibration of the chilean satellite FASat-C using RapidEye and EO-1 hyperion data and a simultaneous nadir overpass approach. *Remote Sens.* **2016**, *8*, 612. [CrossRef]
16. Chander, G.; Hewison, T.J.; Fox, N.; Wu, X.; Xiong, X.; Blackwell, W.J. Overview of Intercalibration of Satellite Instruments. *IEEE Trans. Geosci. Remote Sens.* **2013**, *51*, 1056–1080. [CrossRef]
17. Xu, N.; Chen, L.; Wu, R.H.; Hu, X.Q.; Sun, L.; Zhang, P. In-flight intercalibration of FY-3C visible channels with AQUA MODIS. In Proceedings of the SPIE Asia-Pacific Remote Sensing, Beijing, China, 13–16 October 2014.
18. Heidinger, A.K.; Straka, W.C.; Molling, C.C.; Sullivan, J.T.; Wu, X.Q. Deriving an inter-sensor consistent calibration for the AVHRR solar reflectance data record. *Int. J. Remote Sens.* **2010**, *31*, 6493–6517. [CrossRef]
19. Cao, C.; Weinreb, M.; Xu, H. Predicting simultaneous nadir overpasses among polar-orbiting meteorological satellites for the intersatellite calibration of radiometers. *J. Atmos. Ocean. Technol.* **2004**, *21*, 537–542. [CrossRef]
20. Karlsson, K.G.; Johansson, E. Multi-Sensor Calibration Studies of AVHRR-Heritage Channel Radiances Using the Simultaneous Nadir Observation Approach. *Remote Sens.* **2014**, *6*, 1845–1862. [CrossRef]
21. USGS. USGS EROS Archive—Sentinel-2—Comparison of Sentinel-2 and Landsat. Available online: https://www.usgs.gov/centers/eros/science/usgs-eros-archive-sentinel-2-comparison-sentinel-2-and-landsat?qt-science_center_objects=0#qt-science_center_objects (accessed on 11 February 2020).
22. Stumpf, A.; Michéa, D.; Malet, J.P. Improved Co-Registration of Sentinel-2 and Landsat-8 Imagery for Earth Surface Motion Measurements. *Remote Sens.* **2018**, *10*, 160. [CrossRef]
23. ESA. Sentinel-2. Available online: https://sentinel.esa.int/web/sentinel/missions/sentinel-2 (accessed on 12 February 2020).
24. USGS. Landsat Collection 1. Available online: https://www.usgs.gov/land-resources/nli/landsat/landsat-collection-1?qt-science_support_page_related_con=1#qt-science_support_page_related_con (accessed on 12 February 2020).
25. Irons, J.R.; Dwyer, J.L.; Barsi, J.A. The next Landsat satellite: The Landsat data continuity mission. *Remote Sens. Environ.* **2012**, *122*, 11–21. [CrossRef]
26. European Space Agency (ESA). *Sentinel-2 User Handbook*; Revision 2; ESA Standard Document; ESA: Paris, France, 2015; 64p.
27. USGS. Version 4.0 Landsat 8 Data Users Handbook. Available online: https://www.usgs.gov/media/files/landsat-8-data-users-handbook (accessed on 13 February 2020).
28. ESA. Sentinel-2. Available online: https://sentinel.esa.int/web/sentinel/missions/sentinel-2/satellite-description/orbit (accessed on 13 February 2020).
29. NASA. Landsat 8. Available online: https://satellitesafety.gsfc.nasa.gov/landsat8.html (accessed on 13 February 2020).
30. USGS. Landsat 8 Maneuvers. Available online: https://www.usgs.gov/land-resources/nli/landsat/landsat-8-maneuvers (accessed on 13 February 2020).
31. ESA. Sentinel-2 Operations. Available online: https://www.esa.int/Enabling_Support/Operations/Sentinel-2_operations (accessed on 13 February 2020).
32. Kneubühler, M.; Schaepman, M.E.; Thome, K. Long-term vicarious calibration efforts of MERIS at railroad valley playa (Nevada)—An update. In Proceedings of the Second Working Meeting on MERIS and AATSR Calibration and Geophysical Validation (MAVT-2006), Frascati, Italy, 20–24 March 2006.
33. Rodrigo, J.F.; Gil, J.; Salvador, P.; Gómez, D.; Sanz, J.; Casanova, J.L. Analysis of spatial and temporal variability in Libya-4 with landsat 8 and Sentinel-2 data for optimized ground target location. *Remote Sens.* **2019**, *11*, 2909. [CrossRef]
34. Lillesand, T.; Kiefer, R.W.; Chipman, J. *Remote Sensing and Image Interpretation*; John Wiley & Sons: Hoboken, NJ, USA, 2014.

35. Gascon, F.; Bouzinac, C.; Thépaut, O.; Jung, M.; Francesconi, B.; Louis, J.; Lonjou, V.; Lafrance, B.; Massera, S.; Gaudel-Vacaresse, A.; et al. Copernicus Sentinel-2A calibration and products validation status. *Remote Sens.* **2017**, *9*, 584. [CrossRef]
36. Liang, J.I.; Piper, J.; Tang, J.Y. Erosion and dilation of binary images by arbitrary structuring elements using interval coding. *Pattern Recognit. Lett.* **1989**, *9*, 201–209.
37. Piper, J. Efficient implementation of skeletonisation using interval coding. *Pattern Recognit. Lett.* **1985**, *3*, 389–397. [CrossRef]
38. ESA. Sentinel-2 Products Specification Document. Available online: https://sentinel.esa.int/documents/247904/349490/S2_MSI_Product_Specification.pdf (accessed on 15 February 2020).
39. USGS. Using the USGS Landsat Level-1 Data Product. Available online: https://www.usgs.gov/land-resources/nli/landsat/using-usgs-landsat-level-1-data-product (accessed on 15 February 2020).
40. Buchhorn, M.; Smets, B.; Bertels, L.; Lesiv, M.; Tsendbazar, N.E.; Herold, M.; Fritz, S. *Copernicus Global Land Service: Land Cover 100m: Epoch 2015: Globe*; Version V2.0.2; Zenodo: Geneve, Switzerland, 2019.
41. Neigh, C.S.R.; McCorkel, J.; Middleton, E.M. Quantifying Libya-4 Surface Reflectance Heterogeneity with WorldView-1, 2 and EO-1 Hyperion. *IEEE Geosci. Remote Sens. Lett.* **2015**, *12*, 2277–2281. [CrossRef]
42. ESA. Sentinel-2 L1C Data Quality Report. Available online: https://sentinel.esa.int/documents/247904/685211/Sentinel-2_L1C_Data_Quality_Report (accessed on 27 April 2020).
43. Barsi, J.A.; Alhammoud, B.; Czapla-Myers, J.; Gascon, F.; Haque, M.O.; Kaewmanee, M.; Leigh, L.; Markham, B.L. Sentinel-2A MSI and Landsat-8 OLI radiometric cross comparison over desert sites. *Eur. J. Remote Sens.* **2018**, *51*, 822–837. [CrossRef]
44. ESA. 3rd Sentinel-2 Validation Team Meeting. Available online: https://az659834.vo.msecnd.net/eventsairwesteuprod/production-nikal-public/683987d4267640cba49b0a3e14b89a4e (accessed on 27 April 2020).
45. Zhang, C.; Chen, Y.; Yang, X.; Gao, S.; Li, F.; Kong, A.; Zu, D.; Sun, L. Improved remote sensing image classification based on multi-scale feature fusion. *Remote Sens.* **2020**, *12*, 213. [CrossRef]
46. Sterckx, S.; Wolters, E. Radiometric top-of-atmosphere reflectance consistency assessment for landsat 8/OLI, Sentinel-2/MSI, PROBA-V, and DEIMOS-1 over Libya-4 and RadCalNet calibration sites. *Remote Sens.* **2019**, *11*, 2253. [CrossRef]
47. Sener Aerospace. Seosat/Ingenio. Spanish Earth Observation Satellite. Available online: http://www.aerospace.sener/products/seosat-ingenio-spanish-earth-observation-satellite (accessed on 27 February 2020).
48. Li, J.; Roy, D.P. A global analysis of Sentinel-2a, Sentinel-2b and Landsat-8 data revisit intervals and implications for terrestrial monitoring. *Remote Sens.* **2017**, *9*, 902.

© 2020 by the authors. Licensee MDPI, Basel, Switzerland. This article is an open access article distributed under the terms and conditions of the Creative Commons Attribution (CC BY) license (http://creativecommons.org/licenses/by/4.0/).